Tracking volatile behaviour in sub-volcanic plumbing systems using apatite and glass: insights into pre-eruptive processes at Campi Flegrei, Italy

Michael J. Stock[1,2]*, Madeleine C.S. Humphreys[3], Victoria C. Smith[4], Roberto Isaia[5], Richard A. Brooker[6], David M. Pyle[1]

[1]Department of Earth Sciences, University of Oxford, South Parks Road, Oxford OX1 3AN, UK

[2]Department of Earth Sciences, University of Cambridge, Downing Street, Cambridge CB2 3EQ, UK

[3]Department of Earth Sciences, Durham University, Science Labs, Durham, DH1 3LE, UK

[4]Research Laboratory for Archaeology and the History of Art, University of Oxford, South Parks Road, Oxford OX1 3QY, UK

[5]Istituto Nazionale di Geofisica e Vulcanologia, Osservatorio Vesuviano, via Diocleziano 328, 80154 Napoli, Italy

[6]School of Earth Sciences, University of Bristol, Queens Road, Bristol BS8 1RJ, UK

*E-mail: ms2368@cam.ac.uk

ABSTRACT

Volatile elements play an important role in many aspects of the physicochemical architecture of sub-volcanic plumbing systems, from the liquid line of descent to the dynamics of magma storage and eruption. However, it remains difficult to constrain the behaviour of magmatic

volatiles on short timescales before eruption using established petrologic techniques (e.g. melt inclusions), specifically, in the final days to months of magma storage. This study presents a detailed model of pre-eruptive volatile behaviour in the Campi Flegrei system (Italy), through combined analyses of apatite crystals and glass. The deposits of eight eruptions were examined, covering the full spectrum of melt compositions, eruptive styles and periods of activity at Campi Flegrei in the past 15 kyr. Measured apatite compositions are compared with thermodynamic models that predict the evolution of the crystal compositions during different fractional crystallisation scenarios, including: (i) volatile-undersaturated conditions; (ii) H_2O-saturated conditions; (iii) varying *P*-*T* conditions. The compositions of clinopyroxene-hosted and biotite-hosted apatite inclusions are consistent with crystallisation under volatile-undersaturated conditions that persisted until late in magmatic evolution. Apatite microphenocrysts show significantly more compositional diversity, interpreted to reflect a mixed cargo of crystals derived from volatile-undersaturated melts at depth and melts which have undergone cooling and degassing in discrete shallow-crustal magma bodies. Apatite microphenocrysts from lavas show some re-equilibration during cooling at the surface. Clinopyroxene-hosted melt inclusions within the samples typically contain 2-4 wt % H_2O, indicating that they have been reset during temporary magma storage at 1-3 km depth, similar to the depth of sill emplacement during recent seismic crises at Campi Flegrei. Comparable apatite compositional trends are identified in each explosive eruption analysed, regardless of volume, composition or eruption timing. However, apatites from the different epochs of activity appear to indicate subtle changes in the H_2O content of the parental melt feeding the Campi Flegrei system over time. This study demonstrates the potential utility of integrated apatite and glass analysis for investigating pre-eruptive volatile behaviour in apatite-bearing magmas.

Keywords: Apatite; melt inclusions; Campi Flegrei; volatiles; thermodynamic modelling

INTRODUCTION

Magmatic volatiles (H_2O, CO_2, halogens and SO_2) are minor but important constituents of most silicate melts, and affect almost every aspect of magmatic evolution and eruption. Volatiles influence mineral phase stability and the liquid line of descent (Grove *et al.*, 2003; Zimmer *et al.*, 2010), as well as melt density (Lange & Carmichael, 1990) and viscosity (Giordano *et al.*, 2008), thus exerting a major control on the depths of magma storage and the crustal-scale structure of sub-volcanic systems (Annen *et al.*, 2006). Volatile exsolution and expansion drives volcanic eruptions, and their pre-eruptive behaviour plays an important role in controlling the style and tempo of volcanism at the Earth's surface (Cashman, 2004; Edmonds, 2008; Huppert & Woods, 2002; Roggensack *et al.*, 1997).

Given the fundamental role of volatiles in controlling volcanic processes, quantification of their pre-eruptive concentrations remains a high priority for any investigation. A variety of petrologic methods have been used to decipher the volatile histories of past eruptions, giving access to distinct snapshots of melt volatile contents over variable pre-eruptive timescales. For example, melt inclusions capture a record of magmatic volatiles at the time of entrapment, and have been used widely to constrain volatile concentrations in different magmatic settings (e.g. Dunbar *et al.*, 1989; Saal *et al.*, 2002; Stefano *et al.*, 2011; Wallace, 2005). However, recent studies have revealed the rapidity of H^+ diffusion in common igneous phenocrysts under magmatic conditions, relative to the timescales of pre-eruptive magma storage (e.g. Ingrin & Blanchard, 2006; Reubi *et al.*, 2013; Woods *et al.*, 2000). Melt inclusion H_2O contents may diffusively re-equilibrate through their host crystals within hours to weeks, limiting this volatile record to the very final stages of magma storage and, or, ascent (e.g. Bucholz *et al.*, 2013; Danyushevsky *et al.*, 2002; Gaetani *et al.*, 2012; Lloyd *et al.*, 2013;

Portnyagin *et al.*, 2008; Preece *et al.*, 2014; Reubi *et al.*, 2013). It has also been shown that significant amounts of CO_2 may migrate from the inclusion melt into shrinkage bubbles, leading to underestimates of pressure (Moore *et al.*, 2015). Understanding volatile systematics during late-stage magma storage and the onset of magma ascent is essential for identifying eruption-triggering processes and understanding the 'warning' signs that would be observed at the Earth's surface in the build-up to an eruption.

Apatite [$Ca_4(PO_4)_3F,Cl,OH$] is a common accessory mineral in volcanic, plutonic and ore-forming environments (Piccoli & Candela, 2002) and has received increasing attention as a potential magmatic volatile 'probe', due to its ability to incorporate all major magmatic volatiles into its crystal structure. Halogens and OH are essential structural constituents in apatite and are incorporated as part of a series of exchange equilibria (Candela, 1986; McCubbin *et al.*, 2015). Sulphate and CO_3^{2-} may also substitute into apatite as trace components (e.g. Dietterich & de Silva, 2010; Pan & Fleet, 2002; Riker *et al.*, in press). Recent work has focussed on deciphering the relationship between apatite F-Cl-OH compositions and their host melt volatile contents (e.g. Boyce & Hervig, 2009; Boyce *et al.*, 2014; Candela, 1986; McCubbin *et al.*, 2011; Patiño Douce & Roden, 2006; Piccoli & Candela, 1994; Stock *et al.*, 2016). One advantage of apatite analysis is that phenocryst-hosted apatite inclusions can preserve a record of melt volatile compositions under conditions in which melt inclusions may have re-equilibrated (Stock *et al.*, 2016). Since volatile re-equilibration in mineral-hosted apatite inclusions requires simultaneous diffusion of F, Cl and, or, OH, this process will be rate-limited by halogen diffusivity in the host phenocrysts, which is significantly slower than H^+ (Bucholz *et al.*, 2013; Lloyd *et al.*, 2013). In contrast, F-Cl-OH diffusion within apatite crystals is relatively rapid and microphenocrysts are therefore able to exchange volatiles with their host liquids on geologically short timescales (i.e. microphenocryst rims may re-equilibrate in weeks to years at magmatic temperatures [*T*];

Brenan, 1993). Since these timescales of apatite microphenocryst re-equilibration are longer than timescales of magma ascent (i.e. hours to days), apatite microphenocrysts may preserve a record of pre-eruptive conditions, even when matrix glasses degas at low pressure ([*P*]; Stock *et al*., 2016).

In this study, we investigate apatite and glass compositions in juvenile samples from eight eruptions of the Campi Flegrei volcano (Italy), to determine magmatic volatile systematics and processes in the build-up to eruptions. Campi Flegrei was selected as the focus of this study because its melts are known to be apatite-bearing and volatile-rich (Arienzo *et al.*, 2016; Arienzo *et al.*, 2010; Cannatelli *et al.*, 2007; D'Antonio *et al.*, 1999). It has also recently shown signs of unrest (Chiodini *et al.*, 2012; Moretti *et al.*, 2017). Building on the work of Candela (1986) and Piccoli & Candela (1994) we develop thermodynamic models that predict the theoretical compositional evolution of apatite as a function of changing magma compositions during fractional crystallisation in the presence or absence of different fluid phases. Different populations of apatite inclusions (hosted in biotite and clinopyroxene) and microphenocrysts are identified based on their volatile compositions and, through comparison with our thermodynamic models, we use these to constrain the pattern of magmatic volatile behaviour in the sub-volcanic plumbing system at Campi Flegrei. Although melt inclusions have re-equilibrated during magma ascent, coupled interpretation of apatite and glass compositions provides additional constraints on the structure of the Campi Flegrei plumbing system and the composition of the magmatic fluid phase prior to eruption. Finally, we discuss apparent variations in apatite volatile contents that are linked to different periods of eruptive activity at Campi Flegrei, and suggest that the volatile contents of the incoming parental magmas vary with time.

GEOLOGICAL SETTING

Campi Flegrei comprises a nested caldera system, defined by collapse scarps that formed during the Campanian Ignimbrite (~40 kyr; Giaccio *et al.*, 2017) and Neapolitan Yellow Tuff (NYT, ~15 kyr; Deino *et al.*, 2004) eruptions (Fig. 1). It is one of the most active volcanoes in Europe, having produced >60 eruptions in the past 15 kyr, from vents located within the NYT Caldera (Smith *et al.*, 2011). These are divided into three 'epochs' that represent periods of eruptive activity, separated by prolonged quiescence (Di Vito *et al.*, 1999). Vents for these eruptions are located within the NYT caldera (Fig. 1; Di Vito *et al.*, 1999; Isaia *et al.*, 2009). Epoch 1 occurred from ~15 to 10.6 kyr and produced ~30 explosive eruptions, with a typical inter-eruptive interval of ~70 yrs (Di Vito *et al.*, 1999; Smith *et al.*, 2011). Six low-magnitude explosive eruptions occurred in Epoch 2, between ~9.6 and 9.1 kyr, at an average interval of ~65 yrs (Di Vito *et al.*, 1999; Smith *et al.*, 2011), followed by a long period (~4 kyr) of quiescence. Twenty-seven eruptions occurred within the short Epoch 3 time-period, between ~5.5 and 3.5 kyr (Smith *et al.*, 2011), with an average eruptive interval of ~75 yrs (Di Vito *et al.*, 1999). Most Epoch 3 eruptions were small, explosive events (typically producing 0.02-0.10 km^3 of material, dense rock equivalent [DRE]; Smith *et al*., 2011). However, uniquely within the past 15 kyr, Epoch 3 also includes 4 effusive lava domes (Di Vito *et al.*, 1999; Melluso *et al.*, 1995). The most recent Campi Flegrei eruption was at Monte Nuovo in 1538 CE. This occurred after a >3 kyr dormant period (Piochi *et al.*, 2005), substantially greater than the typical inter-eruption time interval, and is therefore not considered part of Epoch 3 (Smith *et al.*, 2011).

Chemical diversity of eruptive products in the past 15 kyr

The most mafic (shoshonitic) melt inclusions identified in Campi Flegrei typify the mantle melts feeding the system (Mangiacapra *et al.*, 2008; Vetere *et al.*, 2011). Major and trace element studies of Campi Flegrei whole-rocks and glasses show an evolutionary trend from these mafic melts to evolved trachytes or phonolites, with the entire suite formed by fractional crystallisation of a single parental magma composition, punctuated by periodic recharge events (Civetta *et al.*, 1991; D'Antonio *et al.*, 1999; Di Renzo *et al.*, 2011; Di Vito *et al.*, 2011; Fourmentraux *et al.*, 2012; Pappalardo *et al.*, 1999; Smith *et al.*, 2011; Villemant, 1988). Pre-NYT (>15 kyr) melts encompass only the most evolved end of the compositional spectrum (Pappalardo *et al.*, 1999). Post-NYT (<15 kyr) magmas do not follow a continual compositional trend between eruptions (i.e. from primitive to evolved), but the most primitive matrix glasses and whole-rocks are derived from Epoch 1, with Epochs 2 and 3 largely indistinguishable based on their major element compositions (D'Antonio *et al.*, 1999; Smith *et al.*, 2011). Matrix glasses from Monte Nuovo are unlike previous eruptions, with notably higher Na_2O concentrations (Smith *et al.*, 2011).

In contrast, isotopic heterogeneity in Campi Flegrei products suggests that the magmas cannot have formed through fractional crystallisation alone (D'Antonio *et al.*, 2007; Di Renzo *et al.*, 2011; Pappalardo *et al.*, 1999; Pappalardo *et al.*, 2002). The isotopic compositions of <15 kyr Campi Flegrei melts reflect mixing between three distinct end-members, defined by Di Renzo *et al.* (2011) as: the 'NYT component'($^{87}Sr/^{86}Sr$: 0.70750–53, $^{143}Nd/^{144}Nd$: ~0.51246, $^{206}Pb/^{204}Pb$: ~19.04, $\delta^{11}B$: ~ -7.9‰); the 'Minopoli 2 component' ($^{87}Sr/^{86}Sr$: ~0.70860, $^{143}Nd/^{144}Nd$: ~0.51236, $^{206}Pb/^{204}Pb$: ~18.90, $\delta^{11}B$: –7.32‰), and the 'Astroni 6 component' ($^{87}Sr/^{86}Sr$: ~0.70726, $^{143}Nd/^{144}Nd$: ~0.51250, $^{206}Pb/^{204}Pb$: ~19.08, $\delta^{11}B$: -9.8‰). The isotopic composition of Campi Flegrei magmas is defined in the deep crust, before significant crystal fractionation, but the major and trace element compositions of these

primitive liquids must be closely similar to permit evolution along the same liquid line of descent (Pappalardo *et al.*, 2002). The prevalence of these isotopic components correlates with the different epochs of activity: Epochs 1 and 2 show mixing between 'NYT' and 'Minopoli 2' components; Epoch 3 shows mixing between 'NYT', 'Minopoli 2' and 'Astroni 6' components; the Monte Nuovo eruption sampled near end-member 'Astroni 6 component' melts (Di Renzo *et al.*, 2011). Enriched $\delta^{11}B$ in Epochs 1 and 2, reflects a more metasomatised mantle source caused by a higher slab-derived fluid input (D'Antonio *et al.*, 2007) and, or, a lower subducted sediment input into the mantle wedge (Di Renzo *et al.*, 2011; Tonarini *et al.*, 2004). Higher $^{87}Sr/^{86}Sr$ and lower $^{143}Nd/^{144}Nd$ and $^{206}Pb/^{204}Pb$ ratios demonstrate greater crustal assimilation in Epochs 1 and 2 than in Epoch 3 and Monte Nuovo (D'Antonio *et al.*, 2007; Di Renzo *et al.*, 2011). However, the Campi Flegrei liquid line of descent and extent of Sr and Pb isotopic heterogeneity is only compatible with very minor assimilation (D'Antonio *et al.*, 2007, Fowler *et al.*, 2007).

Water contents of Campi Flegrei melt inclusions typically vary from ~1 to ~4 wt % and show no systematic relationship with the degree of magma differentiation (Arienzo *et al.*, 2016; Mangiacapra *et al.*, 2008; Stock *et al.*, 2016). Campi Flegrei melt inclusions generally have very low CO_2 concentrations (<250 ppm), with a few analyses extending up to 400-500 ppm (Arienzo *et al.*, 2016; Arienzo *et al.*, 2010; Marianelli *et al.*, 2006; Stock *et al.*, 2016).

SAMPLES AND METHODS

Eruptions studied

The eruptions investigated cover the full range of melt compositions, eruption sizes and styles of activity from Campi Flegrei in the past 15 kyr (Table 1; see Smith *et al.*, 2011 for full stratigraphy). Vent locations, average matrix glass compositions and absolute eruption ages

for the samples analysed in this study are in given Fig. 1 and Table 1. The Minopoli 1 tuff cone was sampled because it is a small, phono-tephritic to tephri-phonolitic explosive eruption, typical of the early-Epoch 1 eruptions that followed the NYT event (Smith *et al.*, 2011). Scoria was also sampled from the slightly larger, slightly more evolved Pisani 1 eruption, which occurred in mid-late Epoch 1 (Smith *et al.*, 2011). Deposits from more recent eruptions are typically more evolved. We sampled Astroni 1 from Epoch 3, which represents the first of seven small explosive eruptions from the Astroni vent between 4 and 4.4 kyr (Isaia *et al.*, 2004; Smith *et al.*, 2011). These deposits comprise phreatomagmatic surge beds interbedded with subordinate Strombolian pumice layers (Smith *et al.*, 2011). Pomici Principali (PP) was the largest eruption in the last 15 kyr, generating a Plinian column and pyroclastic density currents (Bevilacqua *et al.*, 2016; Di Vito *et al.*, 1999; Smith *et al.*, 2011). These were sampled to investigate relationships between eruption magnitude and apatite volatile compositions. The Baia-Fondi di Baia (B-FdB) and Monte Nuovo eruptions were sampled because they produced highly evolved melts from vents in the western NYT caldera. Baia-Fondi di Baia was the first eruption of Epoch 2 and was particularly explosive, due to magma-H_2O phreatomagmatic interaction, but it only expelled a relatively small volume of material (Pistolesi *et al.*, 2017). The most evolved melts identified in Campi Flegrei were produced in the historic Monte Nuovo tuff cone eruption (Smith *et al.*, 2011). The latitic Santa Maria delle Grazie (SMdG) lava, which is thought to be part of a shallow dyke that fed the SMdG scoria cone (Isaia *et al.*, 2009), and the subsequent trachytic Accademia lava dome (Isaia *et al.*, 2009; Melluso *et al.*, 2012), were sampled to assess differences between apatite volatile compositions in these deposits and explosive units.

Samples

All samples were collected from proximal deposits (Fig. 1), either by Smith *et al.* (2011) or during fieldwork for this study in March 2013 and September 2014. Minopoli 1, PP, Pisani 1,

B-FdB and Astroni 1 samples are CF13, CF6, CF25, CF88 and CF69 of Smith *et al.* (2011). The Astroni 1 sample was investigated by Stock *et al.* (2016). CF88 is from the initial fallout (Baia) phase of the B-FdB eruption (Pistolesi *et al.*, 2017). The Monte Nuovo sample (CF195) is from the upper pyroclastic flow unit (Table 1; Unit II of Piochi *et al.*, 2005) . The SMdG (CF200) and Accademia (CF163) samples were collected from the centre of the NYT caldera.

All samples have the major phase assemblage: K-feldspar + plagioclase + clinopyroxene + biotite + apatite + magnetite. Samples also contain fluorite ± sulphides ± sodalite ± leucite, with precipitation of these accessory phases constrained to late in magmatic evolution by their absence as phenocryst-hosted inclusions in natural samples, and by experimental studies and thermodynamic models (Arzilli *et al.*, 2016; Fowler *et al.*, 2007). Olivine is reported in mafic samples from Campi Flegrei (Cannatelli *et al.*, 2007) but was not observed in this study. Crystal contents are typically <5-30% (from qualitative observations and Isaia *et al.*, 2004; Mastrolorenzo & Pappalardo, 2006; Piochi *et al.*, 2005) but notably lower in B-FdB (<<1%; Mastrolorenzo & Pappalardo, 2006). In Monte Nuovo, two pyroxene populations can be identified in hand specimen: one black and one green, as in other eruptions at Campi Flegrei and Vesuvius (Cioni *et al.*, 1998; D'Antonio *et al.*, 1999). As apatite and melt inclusions show no systematic compositional difference between these pyroxene populations, they are not separated in the following discussion.

Analytical Methods

Clinopyroxene and biotite phenocrysts were hand-picked from the 250-500 μm size fraction in samples from explosive eruptions and the Accademia lava dome. Heavy liquid and magnetic separation techniques were used to extract apatite microphenocrysts from the 44-250 μm size fraction. Crystals and matrix ash grains were mounted in epoxy, ground and

polished for analysis. Lava samples were prepared as polished thin sections. Samples were examined using an FEI Quanta 650 FEG scanning electron microscope (SEM), operating with a 20 kV, ~6-7 nA beam, in the Department of Earth Sciences, University of Oxford. Only apatite inclusions away from cracks and fully enclosed within host phenocrysts were analysed, to ensure that they were trapped during phenocryst growth and were unable to subsequently re-equilibrate with melt or fluids. Melt inclusions were only analysed if they did not show visual evidence for post-entrapment crystallisation and were located away from cracks in their host phenocryst. Ash, lapilli fragments and lavas were also assessed by SEM to identify microlite-free regions for analysis of the matrix glass compositions.

Mineral and glass major, trace and halogen element compositions were analysed using a JEOL 8600 electron microprobe at the Research Laboratory for Archaeology and the History of Art, University of Oxford. Samples were re-polished prior to electron probe microanalysis (EPMA) to remove any compositional modification induced by SEM electron-beam exposure (Stock *et al.*, 2015), and subsequently carbon coated along with secondary standards to avoid variable light element X-ray attenuation. Apatite was analysed using a defocussed (5 μm), 15 kV, 10 nA beam, with halogens analysed first. Where possible, apatite crystals were analysed with the *c*-axis parallel to the plane of the mount. This routine limits the potential for time-dependent variability in halogen X-ray counts during analysis (Goldoff *et al.*, 2012; Stock *et al.*, 2015; Stormer *et al.*, 1993), while maintaining reasonable precision for low-concentration elements (i.e. Cl). In glass, most elements were measured using a defocussed (10 μm), 15 kV, 6 nA beam to minimise Na_2O and SiO_2 migration (e.g. Humphreys *et al.*, 2006); when in low-abundance, SO_2, P_2O_5 and Cl were measured in a second analysis using a 30 nA current. In both crystals and glass, count times were 20-30 s for major elements and 30-90 s for minor elements (120 s for Cl and SO_2 in apatite). Backgrounds were determined by counting for half of the on-peak count time on either side of

the peak. Glass and apatite analytical totals were typically 95-99% and 96-102%, respectively. Data were filtered to remove analyses with totals <92%, and >101.5% in glass. Apatite totals >100% likely reflect minor electron-beam induced compositional modification (Stock *et al.*, 2015) and totals significantly <100% likely result from the absence of trace elements (e.g. REE) in the analytical routine. Apatite OH contents in EPMA data were calculated 'by difference', assuming stoichiometry. Typical analytical uncertainties are reported in Tables 2 and 3.

A subset of apatites and glasses was analysed for H, F and Cl using a Cameca ims-4f secondary ion mass spectrometer (SIMS) at the Edinburgh Ion Micro-Probe Facility, University of Edinburgh, using the methods outlined in Stock *et al.* (2016). Samples were re-polished prior to SIMS analysis to remove any surficial halogen modification induced during EPMA (Stock *et al.*, 2015). In apatite, F, Cl and H_2O concentrations were derived from working curves of $^{19}F/^{44}Ca$ *vs* F, $^{35}Cl/^{44}Ca$ *vs* Cl and $^{1}H/^{44}Ca$ *vs* H_2O, populated by independently characterised apatite standards (Fig. S1). Glass H_2O concentrations were similarly derived from working curves of $^{1}H/^{30}Si$ vs. H_2O populated by well-characterised rhyolitic glasses (Supplementary Data Fig. S2). Working curves were created at the beginning of each day, analytical session or when beam conditions were changed. NIST SRM610 was used as a primary standard for glass F calibration, with ^{44}Ca as the internal standard, based on EPMA of the same spot. SIMS backgrounds were monitored using anhydrous synthetic apatite or clinopyroxene crystals for apatite and glass, respectively. Working curves have a polynomial fit for H_2O in apatite and linear fit for all other elements, with R^2 typically >0.99. Typical analytical uncertainties are reported in Tables 2 and 3.

APATITE AND GLASS COMPOSITIONS

In total, >800 apatite and >250 glass analyses were acquired on samples from the eight Campi Flegrei eruptions (Table 1), using EPMA to identify broad compositional trends (full datasets in Supplementary Data Tables S1, S2; http://www.petrology.oxfordjournals.org) and SIMS to measure a subset of crystals and glasses for H_2O and halogens with lower analytical uncertainties (Tables 2, 3). All glass data in the text and Figs 2, 3 and 4a-d are plotted normalised to 100% anhydrous. All apatite analyses were made close to the centre of the mineral grains. Glass compositions could not be obtained from lava deposits (Table 1), due to melt inclusion devitrification and groundmass crystallisation. Apatite inclusions from these eruptions were excluded as they were not isolated from melt/fluids after entrapment: biotites are partially (in the case of SMdG) or fully (for Accademia) broken down and pyroxenes are heavily fractured, such that all apatite inclusions are touching major cracks or are incompletely enclosed by their host crystals. Baia-Fondi di Baia melt inclusions were too small (typically <20 μm) to analyse by SIMS. Astroni 1 apatite data from Stock *et al.* (2016) were recalibrated using updated standard compositions, resulting in minor modification of absolute compositions but no change to the trends in this dataset. These were included with additional glass and apatite analyses from this eruption.

Glass major element compositions

Melt inclusions and matrix glasses analysed in this study cover a wide compositional range from trachy-basalts and basanites to phonolites and trachytes (Tables 2, Supplementary Data Table S1), encompassing almost the entire compositional diversity reported in <15 kyr Campi Flegrei deposits (Figs 2,3). Clinopyroxene-hosted melt inclusion compositions differ between eruptions: Minopoli 1 melt inclusions are the most mafic (50.46 to 56.84 wt % SiO_2) and cover the largest compositional range; Pisani 1 and PP include the next most mafic melt

inclusions, with SiO_2 as low as 54.18 wt %; melt inclusions from other eruptions are typically phonolitic to trachytic (Fig. 2). The same overall trend is seen for the matrix glasses (Fig. 3), although in general, they are more evolved than melt inclusions from the same eruption, with higher SiO_2 (typically >53 wt %) and alkali element concentrations (Tables 2, S1).

For all elements measured, melt inclusion and matrix glass compositions plot on a single compositional trend, in agreement with literature data (Figs 2, 3). Glass SiO_2, Na_2O and K_2O concentrations typically increase with decreasing MgO, while CaO, FeOt and TiO_2 concentrations decrease (Figs 2, 3; Table 2, Supplementary Data Table S1). However, glass K_2O and SiO_2 concentrations decrease at low MgO contents ($\lesssim$0.5 wt % MgO). Some low-MgO matrix glasses from Monte Nuovo and B-FdB are particularly K_2O-depleted and Na_2O-rich (Fig. 3). This is consistent with fractional crystallisation models, which indicate early fractionation of olivine, clinopyroxene and magnetite (Fowler *et al.*, 2007) but show a major change in compatibility for K_2O and Na_2O at ~0.5 wt % MgO, after plagioclase, biotite and K-feldspar come onto the liquidus (Cannatelli, 2012; Fowler *et al.*, 2007; Stock *et al.*, 2016).

Glass volatile compositions

Campi Flegrei melt inclusions analysed in this study show that Cl generally increases as MgO decreases, consistent with previous analyses (Fig. 4a). Minopoli 1 melt inclusions have the lowest Cl concentrations (0.32 to 0.85 wt %), while melt inclusions from Pisani 1 and PP are intermediate (0.58 to 0.89 wt %). Melt inclusions from other eruptions have higher Cl concentrations, extending up to 1.17 wt % (Fig. 4a; Supplementary Data Table S1). Matrix glass Cl contents are typically similar to melt inclusions; the most Cl-depleted matrix glasses (0.50-0.79 wt %) are from Minopoli 1 and Pisani 1, with the highest Cl concentrations in matrix glasses from Monte Nuovo and B-FdB reaching 1.20 wt % (Fig. 4b; Supplementary Data Table S1). Some low MgO (<0.5 wt %) matrix glasses from Astroni 1 and B-FdB have

low Cl contents (<0.6 wt %), in agreement with the greater variability in matrix glass Cl concentrations at low MgO previously reported in the literature (Fig. 4b).

Mafic (≳2 wt % MgO) melt inclusions from Campi Flegrei show scattered F contents, with concentrations up to 0.46 wt % F in Minopoli 1 (Fig. 4c). In more evolved melt inclusions (≲2 wt % MgO), F is typically higher in inclusions with lower MgO contents, from <0.1 wt % in Pisani 1 and PP to ~0.4 wt % in B-FdB (Fig. 4c; Table S1). Fluorine concentrations up to 0.61 wt % have been reported in very low MgO melt inclusions (Fourmentraux *et al.*, 2012). In general, matrix glass F concentrations are approximately constant (~0.1-0.3 wt %; Fig. 4d). However, F is significantly enriched in low MgO (<0.5 wt %) matrix glasses from Monte Nuovo (typically 0.6-0.8 wt % F), with a single analysis reaching 1.26 wt %.

Melt inclusions analysed in this study typically contain ~2-4 wt % H_2O and show no correlation with MgO (Fig. 4e), consistent with other Campi Flegrei eruptions (Arienzo *et al.*, 2016). Some inclusions have H_2O concentrations as low as 1.04 wt %, with the largest variability at low MgO concentrations (<1.5 wt %), where H_2O concentrations extend to >5 wt %, within the range previously reported for <15 kyr Campi Flegrei eruptions (up to 6.96 wt %; Cannatelli *et al.*, 2007). Matrix glass H_2O contents are lower than in melt inclusions; mafic Minopoli 1 and Pisani 1 matrix glasses consistently have H_2O concentrations <0.4 wt %, whereas more evolved (<1 wt % MgO) PP, Astroni 1 and Monte Nuovo matrix glasses have more variable H_2O concentrations, extending to >1 wt % (Fig. 4f).

Apatite volatile compositions

Apatite inclusions

Clinopyroxene-hosted apatite inclusions have measured F concentrations from 1.86 to 2.92 wt %; Cl concentrations from 0.41 to 1.27 wt % and OH concentrations from 0.39 to 1.42 wt %

(Table 3, Supplementary Data Table S2). This translates to X_{Cl}/X_{OH} ratios from 0.19 to 1.22, X_F/X_{OH} from 1.33 to 5.79 and X_F/X_{Cl} from 2.96 to 12.8 (where X_F, X_{Cl} and X_{OH} are the mole fractions of F, Cl and OH, respectively). Variations in the apatite volatile site can typically be described by an F-OH exchange, with an approximately constant Cl component (Fig. 5a). Baia-Fondi di Baia is an exception, where Cl in clinopyroxene-hosted apatite inclusions is notably depleted relative to inclusions in other eruptions. In general, clinopyroxene-hosted apatite inclusions show a positive correlation between X_{Cl}/X_{OH} and X_F/X_{OH} and approximately constant X_F/X_{Cl} (Figs 5b, c).

Biotite-hosted apatite inclusions have a more restricted compositional range than clinopyroxene-hosted inclusions, with F, Cl and OH ranging from 1.81 to 2.76 wt %, 0.54 to 1.17 wt % and 0.53 to 1.20 wt %, respectively (Tables 3, Supplementary Data S2). This translates to X_{Cl}/X_{OH} ratios from 0.28 to 0.95, X_F/X_{OH} from 1.20 to 4.11 and X_F/X_{Cl} from 3.31 to 9.47. Biotite-hosted inclusions plot on the same compositional trends as clinopyroxene-hosted inclusions (Fig. 5d-f). However, within an individual eruption, biotite-hosted inclusions are typically offset to more OH-rich compositions, with lower X_{Cl}/X_{OH} and X_F/X_{OH} ratios (Tables 3, Supplementary Data S2).

Apatite microphenocrysts

Apatite microphenocrysts show more compositional diversity than inclusions (Figs 5-7), with a small minority of F concentrations measured by EPMA reaching 4.54 wt %. These high F contents are almost exclusively in lava samples (Supplementary Data Table S2) but exceed the maximum stoichiometric limit of 3.76 wt % F (Pyle *et al.*, 2002), likely reflecting electron beam-induced sample damage in near end-member fluorapatite (Goldoff *et al.*, 2012; Stock *et al.*, 2015; Stormer *et al.*, 1993). The highest F concentrations measured by SIMS (3.80 wt %; Table 3) are stoichiometric within analytical uncertainty. In apatite microphenocrysts, the

minimum F concentration is 1.67 wt %, Cl ranges from 0.02 to 1.47 wt % and measured OH concentrations are <1.97 wt % (Tables 3, Supplementary Data S2). This translates to overall X_{Cl}/X_{OH}, X_F/X_{OH} and X_F/X_{Cl} ratios from ~0 to 16.5, 0.86 to 781 and 2.85 to 374, respectively, with $X_{Cl}/X_{OH} \leq 2.27$ and $X_F/X_{OH} \leq 25.8$ in explosive eruptions. Most apatite microphenocrysts sit on the same compositional trends as the inclusions (Figs 6, 7) but typically extend to more OH-rich compositions with lower X_{Cl}/X_{OH} and X_F/X_{OH} ratios. Compositional differences between apatite inclusions and microphenocrysts along this main trend were used by Stock *et al.* (2016) to give temporal context to apatite data from Astroni 1. Two subsidiary sets of apatite microphenocrysts are observed in some explosive eruptions, both with lower Cl contents than the main trend (Figs 6, 7). One has low X_{Cl}/X_{OH} ratios with X_F/X_{OH} and X_F/X_{Cl} ratios that extend to very high values (i.e. in Monte Nuovo, Astroni 1, B-FdB, Pisani 1, PP, Minopoli 1); the other has high X_{Cl}/X_{OH} and X_F/X_{OH} ratios (i.e. in Astroni 1, B-FdB, PP, Minopoli 1). Additionally, a small number of inclusions from Pisani 1 define a trend towards high X_F/X_{OH} at similar X_{Cl}/X_{OH} ratios to the main population (Figs 7d-f). Apatite microphenocrysts from lava deposits (Accademia and SMdG) are distinct; in ternary space they typically show an increasing F component at the expense of Cl, trending first towards the F-Cl join and then curving towards the F apex, but in binary space they are scattered with no discernible trend (Fig. 6g-l).

Differences between eruptions

The SIMS analyses are more precise than the EPMA data, so subtle differences in apatite compositions between eruptions are more clearly resolved. Clinopyroxene- and biotite-hosted apatite inclusions from Epoch 1 eruptions (Minopoli 1, PP and Pisani 1) are typically more OH-rich than those from the more recent Astroni 1 (Epoch 3) and Monte Nuovo eruptions; this translates to lower X_{Cl}/X_{OH} and X_F/X_{OH} and slightly lower X_F/X_{Cl} ratios in apatite inclusions from Epoch 1 than younger eruptions (Fig. 5). The main population of apatite

microphenocrysts from Astroni 1 are also typically more F-rich, with higher X_{Cl}/X_{OH}, X_F/X_{OH} and X_F/X_{Cl} ratios than those from Epoch 1 eruptions. Monte Nuovo microphenocrysts in this population extend to higher X_{Cl}/X_{OH}, X_F/X_{OH} and X_F/X_{Cl} ratios than those from Epoch 1, but cover the entire compositional diversity of the main microphenocryst population from other eruptions (Figs 6, 7). Baia-Fondi di Baia inclusions (Epoch 2) are relatively X_{Cl}/X_{OH} depleted; B-FdB microphenocrysts are compositionally similar to Epoch 1 (i.e. comparable X_{Cl}/X_{OH}) but follow a different evolutionary trajectory. There is more overlap between eruptions in the lower-precision EPMA dataset but it is still clear that apatite inclusions and microphenocrysts from younger eruptions (Astroni 1 and Monte Nuovo) extend to more F-rich compositions, with higher X_{Cl}/X_{OH}, X_F/X_{OH} and X_F/X_{Cl} ratios, than those from Epoch 1 (Figs 5-7).

THERMODYNAMIC FRAMEWORK FOR APATITE VOLATILE INTERPRETATION

The composition of the apatite volatile site is described by a series of exchange equilibria between F, Cl and OH (e.g. Pan & Fleet, 2002), for example:

$$X_{Cl}^{Ap} + X_{OH}^{m} \rightleftharpoons X_{OH}^{Ap} + X_{Cl}^{m} \quad \text{(eq. 1)}$$

X denotes mole fraction in the apatite (Ap) and melt (m) phases. Exchange coefficients (K) for these equilibria are defined as:

$$K_{Cl-OH\,(P,T)}^{Ap/m} = \frac{a_{\mathrm{Cl}}^{\mathrm{Ap}}}{a_{\mathrm{OH}}^{\mathrm{Ap}}} \cdot \frac{a_{\mathrm{OH}}^{\mathrm{m}}}{a_{\mathrm{Cl}}^{\mathrm{m}}} \quad \text{(eq. 2)}$$

where a is activity. The evolution of F, Cl and H_2O concentrations in the melt (i.e., $a_{\mathrm{OH}}^{\mathrm{m}}$ and so on) during fractional crystallisation depends on the nature of both crystal-melt partitioning and fluid-melt exchange. Therefore, we can predict how apatite compositions in equilibrium

with the melt will evolve during different fractional crystallisation scenarios using appropriate experimental K_Ds from the literature.

We have developed a thermodynamic model, relating apatite compositional evolution to changes in the volatile contents of silicate melts during crystallisation in the presence or absence of different magmatic fluids, building on the work of Candela (1986), who treated halogens and H_2O as perfectly incompatible during volatile-undersaturated crystallisation. First, we calculate the evolution of F, Cl and H_2O in the melt due to crystal ± fluid fractionation. We then compute the volatile composition of apatite in equilibrium with the melt at each stage of the crystallisation model. We assume that the apatite solid solution is ideal and that the apatite-melt exchange coefficients are unaffected by the changing melt composition. The validity of these assumptions, definitions of terminology, and the values of key parameters, including mineral-melt and fluid-melt partition coefficients and the solubility of halogens and H_2O in the silicate melt, are discussed in the Supplementary Information. Our approach can be applied generally to determine apatite compositions during fractional crystallisation. The effects of pressure and temperature variations on apatite compositions are also outlined below.

Apatite fractional crystallisation models

The initial melt Cl (C_{Cl}^0) and F (C_{F}^0) concentrations are set at 0.4 wt % and 0.2 wt %, respectively, based on the mafic melt inclusion compositions given in Table 2 and Supplementary Data Table S1. The initial melt H_2O concentration ($C_{\mathrm{H_2O}}^0$) is set at 2.5 wt %, similar to the predicted Campi Flegrei melt H_2O concentration at *apatite-in* from Rhyolite-MELTS (Stock *et al.*, 2016) and initial H_2O concentrations used for modelling by Fowler *et al.* (2007) and Cannatelli (2012).

During volatile-undersaturated crystallisation, the evolution of all volatile components in the melt is described by the Rayleigh equation:

$$C_{\mathrm{i}}^{\mathrm{m}} = C_{\mathrm{i}}^{0} \cdot \varphi^{\bar{D}_{\mathrm{i}}^{\mathrm{c/m}}-1} \quad \text{(eq. 3)}$$

where $C_{\mathrm{i}}^{\mathrm{m}}$ is the concentration of *i* in the melt at a given melt fraction (φ) and $\bar{D}_{\mathrm{i}}^{\mathrm{c/m}}$ is the bulk crystal-melt partition coefficient.

We simulate the onset of saturation with a H_2O-rich fluid by imposing pre-defined H_2O solubility limits ($C_{\mathrm{H_2O}}^{\mathrm{sat}}$), here taken as 7.5 wt % H_2O, which is appropriate for phonolite liquids at 200 MPa (Webster *et al.*, 2014). Once this solubility limit is reached, the H_2O concentration in the melt is held constant to simulate isobaric fractionation (or can be linearly decreased to illustrate the effect of polybaric decompression). Further H_2O that exsolves due to continuing fractionation is assigned to a separate fluid phase, following Candela & Holland (1986), and we calculate the F and Cl concentration of that fluid phase using the fluid-melt partition coefficients (i.e. $D_{\mathrm{F}}^{\mathrm{f/m}}$ and $D_{\mathrm{Cl}}^{\mathrm{f/m}}$, respectively). This fluid is iteratively extracted from the evolving melt by mass balance. We calculate mole fractions of Cl, F and total H_2O in the melt following Li & Hermann (2017) and use the H_2O speciation model of Zhang (1999) for a temperature of 1020 °C to calculate the mole fraction of OH in the melt. Finally, we calculate the mole fraction of F-apatite, Cl-apatite and OH-apatite in equilibrium with the calculated melt composition, following Candela (1986), and thus apatite $X_{\mathrm{Cl}}/X_{\mathrm{OH}}$, $X_{\mathrm{F}}/X_{\mathrm{OH}}$ and $X_{\mathrm{F}}/X_{\mathrm{Cl}}$.

Model outputs: apatite compositional evolution during fractional crystallisation

During volatile-undersaturated crystallisation for a range of parameters (see Supplementary Data), apatite compositions typically show a decrease in both $X_{\mathrm{F}}/X_{\mathrm{OH}}$ and $X_{\mathrm{F}}/X_{\mathrm{Cl}}$ ratios, while $X_{\mathrm{Cl}}/X_{\mathrm{OH}}$ may increase or decrease depending on the exact values of the crystal-melt partition coefficients for F, Cl and OH (Fig. 8b-c). In contrast, H_2O-saturated crystallisation is

characterised by a strong decrease in apatite X_{Cl}/X_{OH} ratios per unit crystallisation, with increasing X_F/X_{Cl} and variable X_F/X_{OH} (Fig. 8e-f). This is because fluid-melt partition coefficients for Cl are typically much higher than for F (Webster *et al*., 2014; Borodulin *et al*., 2009). In ternary space, volatile-undersaturated trajectories are typified by apatite compositional evolution away from the F apex (Fig. 8a). Conversely, during H_2O-saturated crystallisation apatite compositions move towards the F-OH binary (Fig. 8d). Under polybaric H_2O-saturated conditions, where H_2O is lost from the melt during depressurisation, crystal compositions may then curve towards the F apex (Fig. 8d).

The melt volatile composition

Varying the initial melt C_i^0 translates the starting point of the model in apatite compositional space, and changes the relative magnitudes of the calculated variations in apatite volatile components per unit crystallisation. However, the slope or *direction* in binary or ternary space remains the same (Fig. 9a, b). In the general H_2O-saturated case, decreasing $C_{H_2O}^{sat}$ (e.g. at lower pressure or a different melt composition) reduces the extent of volatile-undersaturated crystallisation before second boiling, but does not affect the trajectory of apatite compositional evolution after volatile-saturation is achieved (Fig. 9c, d). Our model does not deal with saturation of either fluorite, which is present only as a late-stage accessory mineral, or brine. Fluorine and Cl act as incompatible elements during fractionation (i.e. higher halogen concentrations in low MgO in glass analyses; Fig. 4a-d), which suggests that brine exsolution is also not a major factor at Campi Flegrei. We would anticipate that formation of fluorite and, or, brine would change the mineral-melt and, or, fluid-melt volatile partition coefficients at the late stages of fractional crystallisation.

Effect of pressure and temperature on apatite composition

As apatite-melt halogen-OH exchange coefficients depend on pressure and temperature (Piccoli & Candela, 1994; Riker *et al.*, in press), mineral compositions may vary, even at a constant melt composition (e.g. Eq. 2). This is not treated in the fractional crystallisation model detailed above but we illustrate the effects of cooling in Fig. 10, using the experimental regression of Riker *et al.* (in press); this is qualitatively consistent with the earlier work of Piccoli & Candela (1994). Cooling drives apatite compositions to higher X_{Cl}/X_{OH}, X_F/X_{OH} and X_F/X_{Cl} ratios, reflecting an increasing preference for the smaller F anion at low temperatures. However, the slope (in binary space) of the cooling trend depends strongly on the Cl concentration of the liquid; at low melt Cl contents, apatite is driven towards high X_F/X_{OH} only (Fig. 10). Pressure has little effect on apatite compositions at constant melt composition (Piccoli & Candela, 1994; Riker *et al.*, in press), with depressurisation primarily allowing a slight increase in the apatite Cl component, which is reflected in a minor decrease in X_F/X_{Cl} and increase in X_{Cl}/X_{OH} ratios.

DISCUSSION

Application of apatite thermodynamic model to Campi Flegrei

The clear differences in model apatite trajectories between H_2O-saturated and volatile-undersaturated conditions (Fig. 8) suggest that apatite may hold significant clues to understanding the late-stage variations in fluid systematics in magmatic-hydrothermal systems.

Texturally-constrained analyses give a temporal dimension to the apatite dataset (Figs 5-7) and analysis of Astroni 1 has shown that the $X_{Halogen}/X_{OH}$ ratios of crystals on the main

compositional trend decrease during magmatic evolution (Stock *et al.*, 2016). The same temporal trend is apparent in all eruptions analysed: apatite inclusions trapped in early-formed clinopyroxene phenocrysts (*clinopyroxene-in* = 1080 °C; Stock *et al*., 2016) extend to higher $X_{\mathrm{Halogen}}/X_{\mathrm{OH}}$ ratios than in late-formed biotite phenocrysts (*biotite-in* = 910 °C; Stock *et al*., 2016). Figure 6a-c shows that a good model fit can be achieved with our natural apatite analyses from Campi Flegrei using $K_{\mathrm{Cl-OH}}^{\mathrm{Ap/m}}$= 25, $K_{\mathrm{F-OH}}^{\mathrm{Ap/m}}$= 75 and $K_{\mathrm{Cl-F}}^{\mathrm{Ap/m}}$= 0.22, which are within the range identified experimentally (Riker *et al.*, in press) and the effects of varying input parameters on the model fit are shown in Figs 8, 9 and Supplementary Data Figs. S3-S6. The model fit (Fig. 6a-c) represents ~70% crystallisation at volatile-undersaturated conditions, with constant crystal-melt partition coefficients $\overline{D}_{\mathrm{F}}^{\mathrm{c/m}}\approx 0.99$, $\overline{D}_{\mathrm{Cl}}^{\mathrm{c/m}}\approx 0.8$ and $\overline{D}_{\mathrm{OH}}^{\mathrm{c/m}}\approx 0.01$ (Figs 6a-c). These are realistic given the increase in glass halogen concentrations with decreasing MgO and the low modal abundance of apatite and biotite. The low $X_{\mathrm{Cl}}/X_{\mathrm{OH}}$ values identified in some apatite microphenocrysts can be partially reproduced by subsequent H_2O-saturated crystallisation, with $\overline{D}_{\mathrm{Cl}}^{\mathrm{f/m}}$ = 20 and $\overline{D}_{\mathrm{F}}^{\mathrm{f/m}} = 0.7$ (Figs 6a-c), consistent with alkali melt-fluid halogen partitioning experiments under magmatic conditions (Borodulin *et al.*, 2009; Signorelli & Carroll, 2000). However, our simple isobaric, isothermal H_2O-saturated crystallisation models cannot reproduce the range of $X_{\mathrm{F}}/X_{\mathrm{OH}}$ ratios observed in the natural low $X_{\mathrm{Cl}}/X_{\mathrm{OH}}$ subsidiary population (Fig. 8d-f). Decompression-induced degassing could account for some of this compositional variability but cooling, after the apatites have re-equilibrated under H_2O-saturated conditions, appears to be the primary mechanism to drive compositions to the very high $X_{\mathrm{F}}/X_{\mathrm{OH}}$ ratios observed in some eruptions (e.g. PP; Figs 7,10). The second, high $X_{\mathrm{Cl}}/X_{\mathrm{OH}}$ and $X_{\mathrm{F}}/X_{\mathrm{OH}}$ subsidiary population (e.g. Minopoli 1) is consistent with re-equilibration of apatites during cooling of a less degassed melt (Fig. 10).

Pre-eruptive volatile behaviour and the structure of the Campi Flegrei magmatic system

Our models reproduce the main compositional trend in apatite inclusions and microphenocrysts through protracted volatile-undersaturated crystallisation (Figs 5-7). This suggests that the main zone of magma storage and crystallisation remained volatile-undersaturated until late in magmatic evolution (i.e. after the entrapment of biotite-hosted inclusions, see Stock *et al.*, 2016) prior to past eruptions at Campi Flegrei. Thermodynamic (Rhyolite-MELTS) fractional crystallisation models, combined with relevant phonolite solubility data, also show that H_2O would remain undersaturated in Campi Flegrei melts until after *biotite-in* (i.e. ~910°C) at pressures ≳150 MPa (Carroll & Blank, 1997; Stock *et al.*, 2016; Webster *et al.*, 2014). Our conclusion that the system remained persistently volatile-undersaturated until a late stage is therefore consistent with independent estimates of Campi Flegrei magma storage conditions, which suggest a high-pressure zone of major melt storage and crystallisation (Fig. 11). Seismic tomography shows that the current region of major melt storage beneath Campi Flegrei is ~1 km thick and at a depth of 7.5 km (Zollo *et al.*, 2008), which would equate to storage pressures of ~170 to 190 MPa. This broadly agrees with phase equilibria models, which indicate that mineral and glass compositions produced in past Campi Flegrei eruptions were stable at pressures between 150 and 300 MPa (i.e. 6.6-13.3 km; Bohrson *et al.*, 2006; Cannatelli, 2012; Fowler *et al.*, 2007) and the volatile contents of melt inclusions from <15 kyrs Campi Flegrei eruptions (Fig. 11), which give saturation pressures up to 229 MPa (~10 km; Arienzo *et al*., 2016 [using a crustal density of 2.3 g/cm^3 after Rosi & Sbrana, 1987]). In particular, magma storage depths inferred from melt inclusion volatile contents for the Agnano-Monte Spina (Arienzo *et al.*, 2010) and Nisida (Arienzo *et al.*, 2016) eruptions overlap at 6.5 to 9.4 km, which agrees very well with the current depth of major magma storage (7.5 to 8.5 km; Zollo *et al.*, 2008). This appears to demonstrate that melt storage and crystallisation before past eruptions occurred at very similar depths to today.

In addition to the main population of apatite inclusions and microphenocrysts, two subsidiary sets of lower-Cl microphenocrysts are present in some eruptions, as discussed above. Apatites with low X_{Cl}/X_{OH} ratios and high X_F/X_{OH} and X_F/X_{Cl} ratios (i.e. in Monte Nuovo, Astroni 1, B-FdB, Pisani 1, PP, Minopoli 1; Figs 6, 7) are consistent with H_2O-saturated fractionation at high $D_{Cl}^{f/m}$, where Cl is efficiently extracted from the melt into the fluid phase, but with cooling following extensive fluid exsolution. This requires equilibrating first with low Cl concentrations in the melt due to degassing, so that any later thermal re-equilibration drives apatites to high X_F/X_{OH} and X_F/X_{Cl} only (Fig. 10). The second subsidiary set of apatites, with elevated X_{Cl}/X_{OH} and/or X_F/X_{OH} ratios (i.e. in Astroni 1, B-FdB, PP, Minopoli 1; Figs 6, 7), are consistent with equilibration during cooling of a melt that is *not* depleted in Cl (i.e. where Cl has not been extracted into an exsolving fluid; Fig. 10).

These compositions represent a small fraction of our dataset, but the analyses are from the cores of microphenocrysts, suggesting that they may have been fully equilibrated under different conditions. In contrast, microphenocrysts that plot on the main trend show no evidence of re-equilibration or overgrowth of new compositions, within the scale of our analyses (Stock *et al*., 2016 checked several grains for compositional zonation within >16 μm of the rim; although we anticipate that fine-scale zonation might be observable using higher-resolution methods). The rapid experimental diffusivities of halogens in apatite (Brenan, 1994) suggests that these few anomalous grains must therefore have been spatially separated within the magmatic system. The simplest interpretation of our data is that the low-X_{Cl}/X_{OH} apatites represent mushy material left over after incomplete evacuation of magma from separate, shallower storage regions (Fig. 11). Small, melt-rich magma bodies at ~2-4 km beneath the current Campi Flegrei have been imaged by seismic tomography (De Siena *et al.*, 2010) and inferred from modelling of long-term ground deformation (Amoruso *et al.*, 2014a), fumarolic gas emissions (Carlino *et al.*, 2015) and heat flow measurements (Di Maio *et al.*,

2015). These shallow magma bodies could derive from emplacement of sills between eruptions; recent seismic crises (1982-1984 and 2011-2013) have been attributed to sill intrusion at 2.75-5 km depth (Fig. 11; Amoruso *et al.*, 2014b;D'Auria *et al.*, 2015; Woo & Kilburn, 2010). Such small, shallow magma bodies would be saturated in volatiles and cooled by interaction with the country rock, allowing microphenocrysts to grow or re-equilibrate. Apatite inclusions, trapped before the magmas were emplaced in the shallow crust, would be 'armoured' by their host phenocrysts, preventing re-equilibration and retaining their volatile-undersaturated signature. Inclusions that were incompletely enclosed by their host phenocrysts do show evidence of diffusional re-equilibration, manifest as depleted Cl contents relative to fully-enclosed inclusions (Stock, 2016). We suggest that magmas ascending from the deep storage region may interact with these shallow melt bodies during eruptions, assimilating some of the residual material and acquiring a mixed cargo of microphenocrysts (Fig. 11). Magmas derived from the deep storage region degassed H_2O during ascent, resulting in low matrix glass H_2O contents (Fig. 4f). Similar F and Cl contents in matrix glasses and melt inclusions (Fig. 4a-d) demonstrate that halogens were not significantly degassed, despite $D_{\mathrm{Cl}}^{\mathrm{f/m}} > 1$ (Signorelli & Carroll, 2000). Relatively undepleted matrix glass Cl concentrations are consistent with kinetically-induced vapour-melt disequilibrium during rapid ascent (Barclay *et al.*, 1996; Shea *et al.*, 2014; Webster *et al.*, 1993).

The apatite microphenocrysts from Pisani 1 that branch away from the main population at moderate $X_{\mathrm{Cl}}/X_{\mathrm{OH}}$ are consistent with cooling (Fig. 10), but before any H_2O-saturated crystallisation has taken place. We suggest that these crystals formed in the main magma storage region at depth, possibly in cooler regions of the reservoir (e.g. close to the walls) and were incorporated before eruption (Fig. 11).

The majority of apatite inclusions and microphenocrysts from B-FdB are compositionally distinct, with significantly lower Cl contents than other explosive eruptions (Figs 5, 7a-c). This could be explained if part of the B-FdB magma crystallised from a melt with a different initial volatile content (i.e. lower Cl, higher H_2O; Fig. 9a, b). Baia-Fondi di Baia occurred at the start of Epoch 2 after a long hiatus in activity (Smith *et al.*, 2011), and may have assimilated some of the country rock surrounding its magma reservoir during this time. Large volumes of residue from the Campanian Ignimbrite magma chamber underlie the Campi Flegrei caldera (D'Antonio, 2011) and represent a potential assimilant. Melt inclusions from the Campanian Ignimbrite extend to high H_2O contents and Campanian Ignimbrite glasses are consistently Cl-deficient compared with eruptions in the past 15 kyrs (cf. Fig. 4a,b; Marianelli *et al.*, 2006; Signorelli *et al.*, 1999). Furthermore, B-FdB glasses are depleted in Sr and Ba and enriched in Zr relative to other <15 kyr eruptions (Smith *et al.*, 2011), again suggesting possible contamination from older (>15 kyr) Campi Flegrei eruptions, including the Campanian Ignimbrite (Tomlinson *et al.*, 2012).

Apatite microphenocrysts from Accademia and SMdG lava samples are distinct from those in explosive deposits. They do not show the same dominant compositional trend of F-OH exchange with an approximately constant Cl, but rather define a trend with an increasing F component at the expense of Cl, curving first towards the F-Cl binary and then towards the F apex (Fig. 6g-l). This is analogous to the modelled trend of apatite compositional evolution during cooling. However, in binary space, apatite microphenocrysts from lava deposits are scattered with no discernible trend. We interpret this as variable extents of diffusive re-equilibration in the lavas (Fig. 10). Although microphenocysts sit on the same cooling trend, they have different starting points and have variably rehomogenised. Such extensive re-equilibration of microphenocryst compositions is unique to lava samples and we interpret that it occurred during slow cooling of the host magma at or near the surface (Fig. 11).

Apatite inclusions in clinopyroxene and biotite record volatile-undersaturated crystallisation (see above) and we would therefore expect the H_2O contents of melt inclusions in the same phenocryst phases to correlate negatively with MgO, as H_2O behaves incompatibly during magmatic evolution. However, there is no correlation between clinopyroxene-hosted melt inclusion H_2O and MgO concentrations in any of the analysed eruptions, and most melt inclusions measured in this study contain ~2.0-3.8 wt % H_2O (Fig. 4e). This may indicate that melt inclusion H_2O contents have been reset after entrapment, reflecting the final (H_2O-saturated) equilibration pressure at shallow crustal levels. Rapid H^+ diffusion through common phenocrysts causes re-equilibration of melt inclusion H_2O concentrations on short timescales (potentially hours to weeks under magmatic conditions) in response to any change in external conditions (e.g. Ingrin & Blanchard, 2006; Reubi *et al.*, 2013; Woods *et al.*, 2000). In contrast, re-equilibration of apatite inclusions would be inhibited by the need for coupled halogen diffusion to retain stoichiometry (Bucholz *et al.*, 2013). Occasional volatile-rich melt inclusions in <15 kyr Campi Flegrei deposits attest to evolved melts at depth (i.e. ≥5 wt % H_2O in Fig. 4e).

Campi Flegrei melt inclusions consistently have very low CO_2 contents (e.g. Arienzo *et al.*, 2010; Marianelli *et al.*, 2006; Stock *et al.*, 2016), so we used a polynomial regression through published 850-950 °C, CO_2-free phonolite and trachyte solubility data (Carroll & Blank, 1997; Di Matteo *et al.*, 2004; Larsen & Gardner, 2004; Schmidt & Behrens, 2008; Webster *et al.*, 2014) to estimate a saturation pressure of ~24-76 MPa for the degassed melt inclusions (2.0-3.8 wt % H_2O). This is equivalent to storage depths of ~1.1-3.4 km, which coincide with the depth of small, melt-rich magma bodies imaged beneath the current Campi Flegrei caldera (~2-4 km; De Siena *et al.*, 2010). We infer that ascending magmas interacted with these shallow melt bodies during eruption, stalling or slowing such that melt inclusions from the deep reservoir re-equilibrated (Fig. 11), and incorporating phenocrysts with degassed

melt inclusions (along with apatite microphenocrysts) which were stored in this shallow crystal reservoir.

Inter-eruption variability in pre-eruptive magma volatile contents

Our data generally show the same qualitative trends in apatite inclusion and microphenocryst compositions in explosive eruptions, regardless of the erupted volume, melt composition or epoch of activity. The majority of apatite inclusions and microphenocrysts plot on a trend that is consistent with volatile-undersaturated fractionation. However, in different eruptions, this main apatite trend is offset depending on the epoch of activity, suggesting a temporal variation in melt volatile composition. This is particularly evident in SIMS data, which are more precise than EPMA. For example, apatite inclusions from Astroni 1 (Epoch 3) and the historical Monte Nuovo eruptions are typically F-rich and OH-depleted with higher $X_{\mathrm{Halogen}}/X_{\mathrm{OH}}$ ratios than those in Epoch 1 (Minopoli 1, PP, Pisani 1; Fig. 5). The same is true for microphenocrysts, except that microphenocrysts from Monte Nuovo cover the entire compositional range measured in other eruptions (Figs 6, 7). Epoch 2 (B-FdB) crystals have similar $X_{\mathrm{Cl}}/X_{\mathrm{OH}}$ ratios to those from Epoch 1 but cannot be compared directly given their distinct compositional trajectory (Fig. 7b,c).

Melt inclusion halogen contents are typically lower in Epoch 1 than in later explosive eruptions (Fig. 4a, c), consistent with the more primitive Epoch 1 major element glass compositions (Figs 2, 3). As $\overline{D}_{\mathrm{F}}^{\mathrm{c/m}} > \overline{D}_{\mathrm{Cl}}^{\mathrm{c/m}} > \overline{D}_{\mathrm{H_2O}}^{\mathrm{c/m}}$ during apatite crystallisation (see Supplementary Data), we would anticipate melt H_2O contents to be proportionally lower for Epoch 1 magmas. Consequently, we would expect apatites forming from the more primitive Epoch 1 magmas to have higher $X_{\mathrm{Halogen}}/X_{\mathrm{OH}}$ than those forming from Epoch 3 magmas, the opposite to what is observed (Fig. 5). This disparity can be explained by a systematic difference in the melt volatile composition at the point of initial apatite crystallization (i.e.

apatite-in; C_i^0), changing apatite compositions without significantly affecting mineral phase stabilities or the trajectory of apatite compositional evolution. Specifically, the change to higher $X_{Halogen}/X_{OH}$ in Astroni 1 (Epoch 3) and Monte Nuovo suggests a decrease in melt H_2O concentrations at *apatite-in* ($C_{H_2O}^0$) relative to Epoch 1 (Fig. 9a, b). At Campi Flegrei, Rhyolite-MELTS models demonstrate that $C_{H_2O}^0$ depends on the H_2O content of the melt at the liquidus, and does not change significantly due to variations in pressure or oxygen fugacity (Stock *et al.*, 2016). Variability in Campi Flegrei apatite compositions from different epochs is therefore likely to reflect temporal variations in the H_2O concentration of parental melts feeding the system; Epoch 1 parental melts have higher apparent H_2O contents than more recent eruptions. This agrees with isotopic evidence, which suggests that Epochs 1 and 2 were fed by the 'Minopoli 2' and 'NYT' end-member (i.e. a high slab-derived fluid and, or, low subducted sediment mantle wedge input) primitive melts, whereas Epoch 3 and Monte Nuovo melts include the 'Astroni 6 end-member' component (i.e. a reduced slab derived fluid and, or, low subducted sediment mantle wedge input; D'Antonio *et al.*, 2007; Di Renzo *et al.*, 2011).

CONCLUSIONS

Apatite analysis represents a robust approach for assessing magmatic volatile behaviour that has many major advantages over established techniques (i.e. melt inclusion analysis). Apatite microphenocrysts remain in equilibrium with their host melts on geologically-short timescales but are unable to re-equilibrate on very short timescales during magma ascent. In contrast, apatite inclusions are isolated from the magma on entrapment and preserve a record of conditions earlier in crystallisation. In explosive Campi Flegrei eruptions, apatite inclusions record persistent volatile-undersaturated conditions until late in the crystallisation history of

the evolving magma, interpreted to occur in a deep magma reservoir at ~7.5-8.5 km, which corresponds with the current depth of major magma storage at Campi Flegrei. In addition to this main volatile-undersaturated trend, apatite microphenocrysts also display subsidiary trends, related to cooling and H_2O-saturated crystallisation. The compositional diversity of apatite microphenocrysts is consistent with a mixed crystal cargo, attained as melts ascending from depth interact with crystal residue in discreet shallow-crustal magma bodies. Clinopyroxene-hosted melt inclusion H_2O contents from Campi Flegrei commonly record saturation pressures equating to 1-3 km depth, due to incorporation of phenocrysts that have been stored in the shallow crust and, or, stalling of ascending magmas as they interact with shallow crustal magma bodies. This corresponds with melt zones imaged seismically beneath the current Campi Flegrei caldera and the depth of sill emplacement during recent seismic crises. In lava deposits, apatite microphenocrysts diffusively re-equilibrate during cooling at the surface. A systematic offset in volatile-undersaturated apatite compositions between eruptions suggest that the H_2O content of parental melts feeding the system was higher in Epoch 1 than in more recent times (i.e. Epoch 3 and Monte Nuovo). Although we have focused on Campi Flegrei, our approach of comparing thermodynamic models of apatite compositional evolution with empirical analyses can be applied widely to determine the temporal evolution of pre-eruptive volatile behaviour in other volcanic systems, providing new perspectives on sub-volcanic processes.

ACKNOWLEDGEMENTS

We thank Richard Hinton, Norman Charnley and Stuart Kearns for analytical assistance and advice, Roel van Elsas for support in mineral separation, and Dan Harlov for generously providing synthetic apatite standard materials. Jason Coumans wrote a MATLAB version of the thermodynamic model which helped in defining the different crystallisation scenarios. The paper was greatly improved by thorough, constructive reviews from Massimo D'Antonio,

Richard Hervig and an anonymous reviewer, and we are grateful to Georg Zellmer for editorial handling. We thank Jenni Barclay and Lars Hansen for their comments on an early iteration of this work and Jim Webster, Jenny Riker and Jon Wade for their valuable feedback and discussion.

FUNDING

M.J.S. was supported by a NERC studentship (NE/K500811/01) and a Junior Research Fellowship from Christ's College, Cambridge. M.C.S.H. was supported by a Royal Society University Research Fellowship. M.C.S.H., V.C.S. and R.B. acknowledge funding from a NERC grant (NE/K003852/1). SIMS analysis was funded by a NERC Edinburgh Ion Microprobe Facility grant (IMF519/0514).

REFERENCES

Amoruso, A., Crescentini, L. & Sabbetta, I. (2014a). Paired deformation sources of the Campi Flegrei caldera (Italy) required by recent (1980–2010) deformation history. *Journal of Geophysical Research: Solid Earth* **119**, 858-879.

Amoruso, A., Crescentini, L., Sabbetta, I., De Martino, P., Obrizzo, F. & Tammaro, U. (2014b). Clues to the cause of the 2011–2013 Campi Flegrei caldera unrest, Italy, from continuous GPS data. *Geophysical Research Letters* **41**, 3081-3088.

Annen, C., Blundy, J. D. & Sparks, R. S. J. (2006). The genesis of intermediate and silicic magmas in deep crustal hot zones. *Journal of Petrology* **47**, 505-539.

Arienzo, I., Mazzeo, F. C., Moretti, R., Cavallo, A. & D'Antonio, M. (2016). Open-system magma evolution and fluid transfer at Campi Flegrei caldera (Southern Italy) during the past

5ka as revealed by geochemical and isotopic data: The example of the Nisida eruption. *Chemical Geology* **427**, 109-124.

Arienzo, I., Moretti, R., Civetta, L., Orsi, G. & Papale, P. (2010). The feeding system of Agnano–Monte Spina eruption (Campi Flegrei, Italy): dragging the past into present activity and future scenarios. *Chemical Geology* **270**, 135-147.

Arzilli, F., Piochi, M., Mormone, A., Agostini, C. & Carroll, M. R. (2016). Constraining pre-eruptive magma conditions and unrest timescales during the Monte Nuovo eruption (1538 ad; Campi Flegrei, Southern Italy): integrating textural and CSD results from experimental and natural trachy-phonolites. *Bulletin of Volcanology* **78**, 72.

Barclay, J., Carroll, M. R., Houghton, B. F. & Wilson, C. J. N. (1996). Pre-eruptive volatile content and degassing history of an evolving peralkaline volcano. *Journal of Volcanology and Geothermal Research* **74**, 75-87.

Bevilacqua, A., Flandoli, F., Neri, A., Isaia, R. & Vitale, S. (2016). Temporal models for the episodic volcanism of Campi Flegrei caldera (Italy) with uncertainty quantification. *Journal of Geophysical Research: Solid Earth* **121**, 7821-7845.

Bohrson, W. A., Spera, F. J., Fowler, S. J., Belkin, H. E., De Vivo, B. & Rolandi, G. (2006). Petrogenesis of the Campanian ignimbrite: implications for crystal-melt separation and open-system processes from major and trace elements and Th isotopic data. *Developments in Volcanology* **9**, 249-288.

Borodulin, G. P., Chevychelov, V. Y. & Zaraysky, G. P. (2009). Experimental study of partitioning of tantalum, niobium, manganese, and fluorine between aqueous fluoride fluid and granitic and alkaline melts. *Doklady Earth Sciences* **427**, 868-873.

Boyce, J. W. & Hervig, R. L. (2009). Apatite as a monitor of late-stage magmatic processes at Volcán Irazú, Costa Rica. *Contributions to Mineralogy and Petrology* **157**, 135-145.

Boyce, J. W., Tomlinson, S. M., McCubbin, F. M., Greenwood, J. P. & Treiman, A. H. (2014). The lunar apatite paradox. *Science* **344**, 400-402.

Brenan, J. (1993). Kinetics of fluorine, chlorine and hydroxyl exchange in fluorapatite. *Chemical Geology* **110**, 195-210.

Bucholz, C. E., Gaetani, G. A., Behn, M. D. & Shimizu, N. (2013). Post-entrapment modification of volatiles and oxygen fugacity in olivine-hosted melt inclusions. *Earth and Planetary Science Letters* **374**, 145-155.

Candela, P. A. (1986). Toward a thermodynamic model for the halogens in magmatic systems: an application to melt-vapor-apatite equilibria. *Chemical Geology* **57**, 289-301.

Candela, P. A. & Holland, H. D. (1986). A mass transfer model for copper and molybdenum in magmatic hydrothermal systems; the origin of porphyry-type ore deposits. *Economic Geology* **81**, 1-19.

Cannatelli, C. (2012). Understanding magma evolution at Campi Flegrei (Campania, Italy) volcanic complex using melt inclusions and phase equilibria. *Mineralogy and Petrology* **104**, 29-42.

Cannatelli, C., Lima, A., Bodnar, R. J., De Vivo, B., Webster, J. D. & Fedele, L. (2007). Geochemistry of melt inclusions from the Fondo Riccio and Minopoli 1 eruptions at Campi Flegrei (Italy). *Chemical Geology* **237**, 418-432.

Carlino, S., Kilburn, C. R. J., Tramelli, A., Troise, C., Somma, R. & De Natale, G. (2015). Tectonic stress and renewed uplift at Campi Flegrei caldera, southern Italy: New insights from caldera drilling. *Earth and Planetary Science Letters* **420**, 23-29.

Carroll, M. R. & Blank, J. G. (1997). The solubility of H_2O in phonolitic melts. *American Mineralogist* **82**, 549-556.

Cashman, K. V. (2004). Volatile controls on magma ascent and eruption. In: Sparks, R. S. J. & Hawkesworth, C. J. (eds.) *The State of the Planet: Frontiers and Challenges in Geophysics*. American Geophysical Union, 109-124.

Chiodini, G., Caliro, S., De Martino, P., Avino, R. & Gherardi, F. (2012). Early signals of new volcanic unrest at Campi Flegrei caldera? Insights from geochemical data and physical simulations. *Geology* **40**, 943-946.

Cioni, R., Marianelli, P. & Santacroce, R. (1998). Thermal and compositional evolution of the shallow magma chambers of Vesuvius: evidence from pyroxene phenocrysts and melt inclusions. *Journal of Geophysical Research: Solid Earth* **103**, 18277-18294.

Civetta, L., Carluccio, E., Innocenti, F., Sbrana, A. & Taddeucci, G. (1991). Magma chamber evolution under the Phlegraean Fields during the last 10 ka: trace element and isotop data. *European Journal of Mineralogy* **3**, 415-428.

D'Antonio, M. (2011). Lithology of the basement underlying the Campi Flegrei caldera: volcanological and petrological constraints. *Journal of Volcanology and Geothermal Research* **200**, 91-98.

D'Antonio, M., Civetta, L., Orsi, G., Pappalardo, L., Piochi, M., Carandente, A., De Vita, S., Di Vito, M. & Isaia, R. (1999). The present state of the magmatic system of the Campi Flegrei caldera based on a reconstruction of its behavior in the past 12 ka. *Journal of Volcanology and Geothermal Research* **91**, 247-268.

D'Antonio, M., Tonarini, S., Arienzo, I., Civetta, L. & Di Renzo, V. (2007). Components and processes in the magma genesis of the Phlegrean Volcanic District, southern Italy. *Geological Society of America Special Papers* **418**, 203-220.

D'Auria, L., Pepe, S., Castaldo, R., Giudicepietro, F., Macedonio, G., Ricciolino, P., Tizzani, P., Casu, F., Lanari, R. & Manzo, M. (2015). Magma injection beneath the urban area of

Naples: a new mechanism for the 2012–2013 volcanic unrest at Campi Flegrei caldera. *Scientific reports* **5**, 13100.

Danyushevsky, L. V., McNeill, A. W. & Sobolev, A. V. (2002). Experimental and petrological studies of melt inclusions in phenocrysts from mantle-derived magmas: an overview of techniques, advantages and complications. *Chemical Geology* **183**, 5-24.

De Siena, L., Del Pezzo, E. & Bianco, F. (2010). Seismic attenuation imaging of Campi Flegrei: Evidence of gas reservoirs, hydrothermal basins, and feeding systems. *Journal of Geophysical Research* **115**, B09312.

Deino, A. L., Orsi, G., de Vita, S. & Piochi, M. (2004). The age of the Neapolitan Yellow Tuff caldera-forming eruption (Campi Flegrei caldera – Italy) assessed by $^{40}Ar/^{39}Ar$ dating method. *Journal of Volcanology and Geothermal Research* **133**, 157-170.

Di Maio, R., Piegari, E., Mancini, C. & Scandone, R. (2015). Numerical study of conductive heat losses from a magmatic source at Phlegraean Fields. *Journal of Volcanology and Geothermal Research* **290**, 75-81.

Di Matteo, V., Carroll, M. R., Behrens, H., Vetere, F. & Brooker, R. A. (2004). Water solubility in trachytic melts. *Chemical Geology* **213**, 187-196.

Di Renzo, V., Arienzo, I., Civetta, L., D'Antonio, M., Tonarini, S., Di Vito, M. A. & Orsi, G. (2011). The magmatic feeding system of the Campi Flegrei caldera: architecture and temporal evolution. *Chemical Geology* **281**, 227-241.

Di Vito, M. A., Arienzo, I., Braia, G., Civetta, L., D'Antonio, M., Di Renzo, V. & Orsi, G. (2011). The Averno 2 fissure eruption: a recent small-size explosive event at the Campi Flegrei Caldera (Italy). *Bulletin of Volcanology* **73**, 295-320.

Di Vito, M. A., Isaia, R., Orsi, G., Southon, J., de Vita, S., D'Antonio, M., Pappalardo, L. & Piochi, M. (1999). Volcanism and deformation since 12,000 years at the Campi Flegrei caldera (Italy). *Journal of Volcanology and Geothermal Research* **91**, 221-246.

Dietterich, H. & de Silva, S. (2010). Sulfur yield of the 1600 eruption of Huaynaputina, Peru: Contributions from magmatic, fluid-phase, and hydrothermal sulfur. *Journal of Volcanology and Geothermal Research* **197**, 303-312.

Dunbar, N. W., Hervig, R. L. & Kyle, P. R. (1989). Determination of pre-eruptive H_2O, F and Cl contents of silicic magmas using melt inclusions: examples from Taupo volcanic center, New Zealand. *Bulletin of Volcanology* **51**, 177-184.

Edmonds, M. (2008). New geochemical insights into volcanic degassing. *Philosophical Transactions of the Royal Society A* **366**, 4559-4579.

Fourmentraux, C., Métrich, N., Bertagnini, A. & Rosi, M. (2012). Crystal fractionation, magma step ascent, and syn-eruptive mingling: the Averno 2 eruption (Phlegraean Fields, Italy). *Contributions to Mineralogy and Petrology* **163**, 1121-1137.

Fowler, S. J., Spera, F. J., Bohrson, W. A., Belkin, H. E. & De Vivo, B. (2007). Phase equilibria constraints on the chemical and physical evolution of the Campanian Ignimbrite. *Journal of Petrology* **48**, 459-493.

Gaetani, G. A., O'Leary, J. A., Shimizu, N., Bucholz, C. E. & Newville, M. (2012). Rapid reequilibration of H_2O and oxygen fugacity in olivine-hosted melt inclusions. *Geology* **40**, 915-918.

Giaccio, B., Hajdas, I., Isaia, R., Deino, A. & Nomade, S. (2017). High-precision 14C and 40Ar/39Ar dating of the Campanian Ignimbrite (Y-5) reconciles the time-scales of climatic-cultural processes at 40 ka. *Scientific reports* **7**, 45940.

Giordano, D., Russell, J. K. & Dingwell, D. B. (2008). Viscosity of magmatic liquids: a model. *Earth and Planetary Science Letters* **271**, 123-134.

Goldoff, B., Webster, J. D. & Harlov, D. E. (2012). Characterization of fluor-chlorapatites by electron probe microanalysis with a focus on time-dependent intensity variation of halogens. *American Mineralogist* **97**, 1103-1115.

Grove, T. L., Elkins-Tanton, L. T., Parman, S. W., Chatterjee, N., Müntener, O. & Gaetani, G. A. (2003). Fractional crystallization and mantle-melting controls on calc-alkaline differentiation trends. *Contributions to Mineralogy and Petrology* **145**, 515-533.

Humphreys, M. C. S., Kearns, S. L. & Blundy, J. D. (2006). SIMS investigation of electron-beam damage to hydrous, rhyolitic glasses: Implications for melt inclusion analysis. *American Mineralogist* **91**, 667-679.

Huppert, H. E. & Woods, A. W. (2002). The role of volatiles in magma chamber dynamics. *Nature* **420**, 493-495.

Ingrin, J. & Blanchard, M. (2006). Diffusion of hydrogen in minerals. *Reviews in Mineralogy and Geochemistry* **62**, 291-320.

Isaia, R., D'Antonio, M., Dell'Erba, F., Di Vito, M. & Orsi, G. (2004). The Astroni volcano: the only example of closely spaced eruptions in the same vent area during the recent history of the Campi Flegrei caldera (Italy). *Journal of Volcanology and Geothermal Research* **133**, 171-192.

Isaia, R., Marianelli, P. & Sbrana, A. (2009). Caldera unrest prior to intense volcanism in Campi Flegrei (Italy) at 4.0 ka BP: Implications for caldera dynamics and future eruptive scenarios. *Geophysical Research Letters* **36**, L21303.

Lange, R. L. & Carmichael, I. S. E. (1990). Thermodynamic properties of silicate liquids with emphasis on density, thermal expansion and compressibility. *Reviews in Mineralogy and Geochemistry* **24**, 25-64.

Larsen, J. F. & Gardner, J. E. (2004). Experimental study of water degassing from phonolite melts: implications for volatile oversaturation during magmatic ascent. *Journal of Volcanology and Geothermal Research* **134**, 109-124.

Li, H. & Hermann, J. (2017). Chlorine and fluorine partitioning between apatite and sediment melt at 2.5 GPa, 800 °C: A new experimentally derived thermodynamic model. *American Mineralogist* **102**, 580-594.

Lloyd, A. S., Plank, T., Ruprecht, P., Hauri, E. H. & Rose, W. (2013). Volatile loss from melt inclusions in pyroclasts of differing sizes. *Contributions to Mineralogy and Petrology* **165**, 129-153.

Mangiacapra, A., Moretti, R., Rutherford, M., Civetta, L., Orsi, G. & Papale, P. (2008). The deep magmatic system of the Campi Flegrei caldera (Italy). *Geophysical Research Letters* **35**, L21304.

Marianelli, P., Sbrana, A. & Proto, M. (2006). Magma chamber of the Campi Flegrei supervolcano at the time of eruption of the Campanian Ignimbrite. *Geology* **34**, 937-940.

Mastrolorenzo, G. & Pappalardo, L. (2006). Magma degassing and crystallization processes during eruptions of high-risk Neapolitan-volcanoes: Evidence of common equilibrium rising processes in alkaline magmas. *Earth and Planetary Science Letters* **250**, 164-181.

McCubbin, F. M., Jolliff, B. L., Nekvasil, H., Carpenter, P. K., Zeigler, R. A., Steele, A., Elardo, S. M. & Lindsley, D. H. (2011). Fluorine and chlorine abundances in lunar apatite: Implications for heterogeneous distributions of magmatic volatiles in the lunar interior. *Geochimica et Cosmochimica Acta* **75**, 5073-5093.

McCubbin, F. M., Kaaden, K. E. V., Tartèse, R., Boyce, J. W., Mikhail, S., Whitson, E. S., Bell, A. S., Anand, M., Franchi, I. A., Wang, J. & Hauri, E. H. (2015). Experimental investigation of F, Cl, and OH partitioning between apatite and Fe-rich basaltic melt at 1.0–1.2 GPa and 950–1000 °C. *American Mineralogist* **100**, 1790-1802.

Melluso, L., De'Gennaro, R., Fedele, L., Franciosi, L. & Morra, V. (2012). Evidence of crystallization in residual, Cl–F-rich, agpaitic, trachyphonolitic magmas and primitive Mg-

rich basalt–trachyphonolite interaction in the lava domes of the Phlegrean Fields (Italy). *Geological Magazine* **149**, 532-550.

Melluso, L., Morra, V., Perrotta, A., Scarpati, C. & Adabbo, M. (1995). The eruption of the Breccia Museo (Campi Flegrei, Italy): Fractional crystallization processes in a shallow, zoned magma chamber and implications for the eruptive dynamics. *Journal of Volcanology and Geothermal Research* **68**, 325-339.

Moore, L., Gazel, E., Tuohy, R., Lloyd, A., Esposito, R., Steele-MacInnis, M., Hauri, E. H., Wallace, P. J., Plank, T. & Bodnar, R. J. (2015). Bubbles matter: An assessment of the contribution of vapour bubbles to melt inclusion volatile budgets. *American Mineralogist* **100**, 806-823.

Moretti, R., De Natale, G. & Troise, C. (2017). A geochemical and geophysical reappraisal to the significance of the recent unrest at Campi Flegrei caldera (Southern Italy). *Geochemistry, Geophysics, Geosystems* **18**, 1244-1269.

Pan, Y. & Fleet, M. E. (2002). Compositions of the apatite-group minerals: substitution mechanisms and controlling factors. *Reviews in Mineralogy and Geochemistry* **48**, 13-49.

Pappalardo, L., Civetta, L., d'Antonio, M., Deino, A., Di Vito, M., Orsi, G., Carandente, A., De Vita, S., Isaia, R. & Piochi, M. (1999). Chemical and Sr-isotopical evolution of the Phlegraean magmatic system before the Campanian Ignimbrite and the Neapolitan Yellow Tuff eruptions. *Journal of Volcanology and Geothermal Research* **91**, 141-166.

Pappalardo, L., Piochi, M., D'Antonio, M., Civetta, L. & Petrini, R. (2002). Evidence for multi-stage magmatic evolution during the past 60 kyr at Campi Flegrei (Italy) deduced from Sr, Nd and Pb isotope data. *Journal of Petrology* **43**, 1415-1434.

Patiño Douce, A. E. & Roden, M. (2006). Apatite as a probe of halogen and water fugacities in the terrestrial planets. *Geochimica et Cosmochimica Acta* **70**, 3173-3196.

Piccoli, P. & Candela, P. (1994). Apatite in felsic rocks: a model for the estimation of initial halogen concentrations in the Bishop Tuff (Long Valley) and Tuolumne Intrusive Suite (Sierra Nevada Batholith) magmas. *American Journal of Science* **294**, 92-135.

Piccoli, P. M. & Candela, P. A. (2002). Apatite in igneous systems. *Reviews in Mineralogy and Geochemistry* **48**, 255-292.

Piochi, M., Mastrolorenzo, G. & Pappalardo, L. (2005). Magma ascent and eruptive processes from textural and compositional features of Monte Nuovo pyroclastic products, Campi Flegrei, Italy. *Bulletin of Volcanology* **67**, 663-678.

Pistolesi, M., Bertagnini, A., Di Roberto, A., Isaia, R., Vona, A., Cioni, R. & Giordano, G. (2017). The Baia–Fondi di Baia eruption at Campi Flegrei: stratigraphy and dynamics of a multi-stage caldera reactivation event. *Bulletin of Volcanology* **79**, 67.

Portnyagin, M., Almeev, R., Matveev, S. & Holtz, F. (2008). Experimental evidence for rapid water exchange between melt inclusions in olivine and host magma. *Earth and Planetary Science Letters* **272**, 541-552.

Preece, K., Gertisser, R., Barclay, J., Berlo, K., Herd, R. A. & EIMF. (2014). Pre-and syn-eruptive degassing and crystallisation processes of the 2010 and 2006 eruptions of Merapi volcano, Indonesia. *Contributions to Mineralogy and Petrology* **168**, 1061.

Pyle, J. M., Spear, F. S. & Wark, D. A. (2002). Electron microprobe analysis of REE in apatite, monazite and xenotime: protocols and pitfalls. *Reviews in Mineralogy and Geochemistry* **48**, 337-362.

Reimer, P. J., Bard, E., Bayliss, A., Beck, J. W., Blackwell, P. G., Bronk Ramsey, C., Buck, C. E., Cheng, H., Edwards, R. L., Friedrich, M., Grootes, P. M., Guilderson, T. P., Haflidason, H., Hajdas, I., Hatté, C., Heaton, T., Hoffmann, D. L., Hogg, A. G., Hughen, K. A., Kaiser, K. F., Kromer, B., Manning, S. W., Niu, M., Reimer, R. W., Richards, D. A., Scott, E. M., Southon, J. R., Staff, R. A., Turney, C. S. M. & van der Plicht, J. (2013).

IntCal13 and Marine13 radiocarbon age calibration curves 0-50,000 years cal BP. *Radiocarbon* **55**, 1869-1887.

Reubi, O., Blundy, J. & Varley, N. R. (2013). Volatiles contents, degassing and crystallisation of intermediate magmas at Volcan de Colima, Mexico, inferred from melt inclusions. *Contributions to Mineralogy and Petrology* **165**, 1087-1106.

Riker, J., Humphreys, M. C. S., Brooker, R. A., De Hoog, J. C. M. & EIMF. (in press). Experimental constraints on H-C-F-Cl partitioning between apatite and silicate melts. *American Mineralogist*.

Roggensack, K., Hervig, R. L., McKnight, S. B. & Williams, S. N. (1997). Explosive basaltic volcanism from Cerro Negro volcano: influence of volatiles on eruptive style. *Science* **277**, 1639-1642.

Rosi, M. & Sbrana, A. (1987). The Phlegrean Fields: CNR. *Quaderni de la Recerca Scientifica* **114**, 1-175.

Saal, A. E., Hauri, E. H., Langmuir, C. H. & Perfit, M. R. (2002). Vapour undersaturation in primitive mid-ocean-ridge basalt and the volatile content of Earth's upper mantle. *Nature* **419**, 451-455.

Schmidt, B. C. & Behrens, H. (2008). Water solubility in phonolite melts: Influence of melt composition and temperature. *Chemical Geology* **256**, 259-268.

Shea, T., Hellebrand, E., Gurioli, L. & Tuffen, H. (2014). Conduit-to localized-scale degassing during Plinian Eruptions: Insights from major element and volatile (Cl and H_2O) analyses within Vesuvius AD 79 pumice. *Journal of Petrology* **55**, 315-344.

Signorelli, S. & Carroll, M. R. (2000). Solubility and fluid-melt partitioning of Cl in hydrous phonolitic melts. *Geochimica et Cosmochimica Acta* **64**, 2851-2862.

Signorelli, S., Vaggelli, G., Francalanci, L. & Rosi, M. (1999). Origin of magmas feeding the Plinian phase of the Campanian Ignimbrite eruption, Phlegrean Fields (Italy): constraints

based on matrix-glass and glass-inclusion compositions. *Journal of Volcanology and Geothermal Research* **91**, 199-220.

Smith, V. C., Isaia, R. & Pearce, N. J. G. (2011). Tephrostratigraphy and glass compositions of post-15 kyr Campi Flegrei eruptions: implications for eruption history and chronostratigraphic markers. *Quaternary Science Reviews* **30**, 3638-3660.

Stefano, C. J., Mukasa, S. B., Andronikov, A. & Leeman, W. P. (2011). Water and other volatile systematics of olivine-hosted melt inclusions from the Yellowstone hotspot track. *Contributions to Mineralogy and Petrology* **161**, 615-633.

Stock, M. J. (2016). The volatile history of past volcanic eruptions. PhD thesis, University of Oxford.

Stock, M. J., Humphreys, M. C. S., Smith, V. C., Isaia, R. & Pyle, D. M. (2016). Late-stage volatile saturation as a potential trigger for explosive volcanic eruptions. *Nature Geoscience* **9**, 249-254.

Stock, M. J., Humphreys, M. C. S., Smith, V. C., Johnson, R. D., Pyle, D. M. & EIMF. (2015). New constraints on electron-beam induced halogen migration in apatite. *American Mineralogist* **100**, 281-293.

Stormer, J. C., Pierson, M. L. & Tacker, R. C. (1993). Variation of F and Cl X-ray intensity due to anisotropic diffusion in apatite. *American Mineralogist* **78**, 641-648.

Tomlinson, E. L., Arienzo, I., Civetta, L., Wulf, S., Smith, V. C., Hardiman, M., Lane, C. S., Carandente, A., Orsi, G., Rosi, M., Müller, W. & Menzies, M. A. (2012). Geochemistry of the Phlegraean Fields (Italy) proximal sources for major Mediterranean tephras: Implications for the dispersal of Plinian and co-ignimbritic components of explosive eruptions. *Geochimica et Cosmochimica Acta* **93**, 102-128.

Tonarini, S., Leeman, W. P., Civetta, L., D'antonio, M., Ferrara, G. & Necco, A. (2004). B/Nb and $\delta^{11}B$ systematics in the Phlegrean Volcanic District, Italy. *Journal of Volcanology and Geothermal Research* **133**, 123-139.

Vetere, F., Botcharnikov, R. E., Holtz, F., Behrens, H. & De Rosa, R. (2011). Solubility of H_2O and CO_2 in shoshonitic melts at 1250 °C and pressures from 50 to 400 MPa: Implications for Campi Flegrei magmatic systems. *Journal of Volcanology and Geothermal Research* **202**, 251-261.

Villemant, B. (1988). Trace element evolution in the Phlegrean Fields (Central Italy): fractional crystallization and selective enrichment. *Contributions to Mineralogy and Petrology* **98**, 169-183.

Vitale, S. & Isaia, R. (2014). Fractures and faults in volcanic rocks (Campi Flegrei, southern Italy): insight into volcano-tectonic processes. *International Journal of Earth Sciences* **103**, 801-819.

Wallace, P. J. (2005). Volatiles in subduction zone magmas: concentrations and fluxes based on melt inclusion and volcanic gas data. *Journal of Volcanology and Geothermal Research* **140**, 217-240.

Webster, J. D., Goldoff, B., Sintoni, M. F., Shimizu, N. & De Vivo, B. (2014). C–O–H–Cl–S–F volatile solubilities, partitioning, and mixing in phonolitic–trachytic melts and aqueous–carbonic vapor ± saline liquid at 200 MPa. *Journal of Petrology* **55**, 2217-2248.

Webster, J. D., Taylor, R. P. & Bean, C. (1993). Pre-eruptive melt composition and constraints on degassing of a water-rich pantellerite magma, Fantale volcano, Ethiopia. *Contributions to Mineralogy and Petrology* **114**, 53-62.

Woo, J. Y. L. & Kilburn, C. R. J. (2010). Intrusion and deformation at Campi Flegrei, southern Italy: Sills, dikes, and regional extension. *Journal of Geophysical Research* **115**, B12210.

Woods, S. C., Mackwell, S. & Dyar, D. (2000). Hydrogen in diopside: diffusion profiles. *American Mineralogist* **85**, 480-487.

Zhang, Y. (1999). H_2O in rhyolitic glasses and melts: Measurement, speciation, solubility, and diffusion. *Reviews of Geophysics* **37**, 493-516.

Zimmer, M. M., Plank, T., Hauri, E. H., Yogodzinski, G. M., Stelling, P., Larsen, J., Singer, B., Jicha, B., Mandeville, C. & Nye, C. J. (2010). The role of water in generating the calc-alkaline trend: new volatile data for Aleutian magmas and a new tholeiitic index. *Journal of Petrology* **51**, 2411-2444.

Zollo, A., Maercklin, N., Vassallo, M., Dello Iacono, D., Virieux, J. & Gasparini, P. (2008). Seismic reflections reveal a massive melt layer feeding Campi Flegrei caldera. *Geophysical Research Letters* **35**, L12306.

FIGURE CAPTIONS

Figure 1. Simplified geological map of the Campi Flegrei caldera showing major structural features, adapted from Vitale & Isaia (2014). The locations of sampling sites (black squares) and vents for each eruption analysed in this study (Table 1) are indicated.

Figure 2. Clinopyroxene-hosted melt inclusion major element compositions from explosive Campi Flegrei eruptions. All data were measured by EPMA and are normalised to 100%. Data are distinguished by eruption (see legend). Grey points show a compilation of literature clinopyroxene- and olivine-hosted melt inclusion compositions in <15 kyr Campi Flegrei deposits from Cannatelli *et al.* (2007), Mangiacapra *et al.* (2008), Arienzo *et al.* (2010), Arienzo *et al.* (2016) and Fourmentraux *et al.* (2012).

Figure 3. Matrix glass major element compositions from explosive Campi Flegrei eruptions. All data were measured by EPMA and are normalised to 100%. Data are distinguished by eruption (see legend in Fig. 2). Grey points are literature matrix glass compositions in <15 kyr Campi Flegrei deposits from Smith *et al.* (2011).

Figure 4. Halogens (a-d) and H_2O (e, f) *versus* MgO compositions in melt inclusions (a,c,e) and matrix glasses (b,d,f) from explosive Campi Flegrei eruptions. MgO and Cl were measured by EPMA (points with no outlines). F and H_2O were measured by SIMS (points with grey outlines). The red dashed lines show EPMA F detection limits of 0.09 wt %. Data in (a-d) are normalised to 100%. Data are distinguished by eruption (see legend in Fig. 2). Grey circles show literature melt inclusion and matrix glass compositions in <15 kyr Campi Flegrei deposits, from the same sources as Figs 2 and 3, respectively. The grey crosses show the compositions of Campanian Ignimbrite melt inclusions and matrix glasses from Signorelli *et al.* (1999).

Figure 5. Volatile compositions of clinopyroxene- (a-c) and biotite-hosted (d-f) apatite inclusions from explosive Campi Flegrei eruptions. Data are presented both in ternary space (a,d) and on binary plots of X_{Cl}/X_{OH} *versus* X_F/X_{OH} (b,e) and X_{Cl}/X_{OH} *versus* X_F/X_{Cl} (c,f). Points with black outlines were measured by SIMS and points without outlines were measured by EPMA. Data are distinguished by eruption (see legend in Fig. 2). The coloured fields highlight EPMA and SIMS data from Epoch 1 (red), and Astroni 1 (Epoch 3) and the historic Monte Nuovo eruptions (blue).

Figure 6. Volatile compositions of apatite microphenocrysts from the historic Monte Nuovo (a-c) and Epoch 3 (d-l) eruptions of Campi Flegrei. Data are presented both in ternary space (a,d,g,j) and on binary plots of X_{Cl}/X_{OH} *versus* X_F/X_{OH} (b,e,h,k) and X_{Cl}/X_{OH} *versus* X_F/X_{Cl} (c,f,i,l). Inset in c shows an expansion of the area outlined by the black dashed box in the

main panel. Points with black outlines were measured by SIMS and points without outlines were measured by EPMA. Non-stoichiometric analyses with F >3.76 wt % (i.e. in lava deposits) are plotted as end-member fluorapatite, with non-stoichiometry likely due to F migration during EPMA (Goldoff *et al.*, 2012; Stock *et al.*, 2015; Stormer *et al.*, 1993). Data are distinguished by eruption (see headings). Lines in (a-c) show the theoretical trajectory of apatite compositional evolution predicted by our thermodynamic model that best fits natural apatite compositions from Campi Flegrei. C_{Cl}^{0}= 0.4 wt %, C_{F}^{0}= 0.2 wt %, $C_{\mathrm{H_2O}}^{0}$= 2.5 wt %, $K_{\mathrm{Cl-F}}^{\mathrm{ap-m}} = 0.22$, $K_{\mathrm{Cl-OH}}^{\mathrm{ap-m}} = 25$, $K_{\mathrm{F-OH}}^{\mathrm{ap-m}} = 75$, $\overline{D}_{\mathrm{F}}^{\mathrm{c/m}}$= 0.99, $\overline{D}_{\mathrm{Cl}}^{\mathrm{c/m}}$= 0.8 and $\overline{D}_{\mathrm{H_2O}}^{\mathrm{c/m}}$= 0.01. H_2O speciation is calculated after Zhang (1999) for a temperature of 1020 °C. The black solid line shows modelled apatite compositional evolution during ~70% volatile-undersaturated crystallisation. The grey lines show modelled apatite compositional evolution during subsequent H_2O-saturated crystallisation, with $D_{\mathrm{Cl}}^{\mathrm{f/m}}$= 20 and $D_{\mathrm{Cl}}^{\mathrm{f/m}}$= 0.7, after $C_{\mathrm{H_2O}}^{\mathrm{m}}$ concentration reaches $C_{\mathrm{H_2O}}^{\mathrm{sat}}$ at 7.5 wt %. The grey line types illustrate the difference between isobaric (0% H_2O loss; solid lines) H_2O-saturated crystallisation and polybaric H_2O-saturated crystallisation with 0.15 wt % (dashed lines) and 0.25 wt % (dotted lines) H_2O loss from the melt into the fluid phase per percent crystallisation.

Figure 7. Volatile compositions of apatite microphenocrysts from Epoch 2 (Baia-Fondi di Baia; a-c) and Epoch 1 (d-l) Campi Flegrei eruptions. Data are presented both in ternary space (a,d,g,j) and on binary plots of $X_{\mathrm{Cl}}/X_{\mathrm{OH}}$ *versus* $X_{\mathrm{F}}/X_{\mathrm{OH}}$ (b,e,h,k) and $X_{\mathrm{Cl}}/X_{\mathrm{OH}}$ *versus* $X_{\mathrm{F}}/X_{\mathrm{Cl}}$ (c,f,i,l). Insets in (c), (f), (i) and (l) show expansions of the areas outlined by the black dashed boxes in the main panels. Points with black outlines were measured by SIMS and points without outlines were measured by EPMA. Data are distinguished by eruption (see headings).

Figure 8. Theoretical apatite compositional trajectories for different crystallisation scenarios (not specific to Campi Flegrei). Data are presented both in ternary (a,d) space and on binary

plots of X_{Cl}/X_{OH} *versus* X_F/X_{OH} (b,e) and X_{Cl}/X_{OH} *versus* X_F/X_{Cl} (c,f). In all models, C_{Cl}^0= 0.4 wt %, C_F^0= 0.2 wt %, $C_{H_2O}^0$= 2.9 wt %, $K_{Cl-F}^{ap-m} = 0.22$, $K_{Cl-OH}^{ap-m} = 25$, $K_{F-OH}^{ap-m} = 75$ and apatite crystallisation begins at the black point (see discussion of input parameters in the text). H_2O speciation is calculated after Zhang (1999) for a temperature of 1020 °C. (a-c) Apatite compositional evolution during volatile-undersaturated fractional crystallisation. Crystal compositions evolve in the arrow direction until 85% crystallisation. Curves show the effect of varying $\overline{D}_i^{c/m}$, where $\overline{D}_F^{c/m} > \overline{D}_{Cl}^{c/m} > \overline{D}_{H_2O}^{c/m}$ and $1 > \overline{D}_i^{c/m} > 0$. Line colours distinguish models with different $\overline{D}_{Cl}^{c/m}$ values (see legend in (c)). Line types distinguishes models with $\overline{D}_F^{c/m} = 0.99$ (solid lines), $\overline{D}_F^{c/m} = 0.5$ (dashed lines) and $\overline{D}_F^{c/m} = 0.14$ (dotted lines). $\overline{D}_{H_2O}^{c/m}$ is set at 0.003; varying $\overline{D}_{H_2O}^{c/m}$ affects crystal X_F/X_{OH} and X_{Cl}/X_{OH} evolution in the opposing sense to $\overline{D}_F^{c/m}$and $\overline{D}_{Cl}^{c/m}$. (d-f) Apatite compositional evolution during H_2O-saturated fractional crystallisation. The black arrow shows an arbitrary trajectory of apatite compositional evolution under volatile-undersaturated conditions ($\overline{D}_F^{c/m} = 0.8$, $\overline{D}_{Cl}^{c/m} = 0.65$, $\overline{D}_{H_2O}^{c/m} = 0.001$), until 61% crystallisation. Water saturates at 61% crystallisation when $C_{H_2O}^m = C_{H_2O}^s = 7.5$ wt % (see Supplementary Data) and crystal compositions continue to evolve in the arrow direction to 85% crystallisation. Line colours distinguish H_2O-saturated models with varying $D_{Cl}^{f/m}$ within a realistic range (see legend in f). $D_{Cl}^{f/m} = 4$ equates to the lowest value measured for phonolitic systems at 150 MPa by Signorelli & Carroll (2000) and apatite trajectories at $D_{Cl}^{f/m} > 50$ are almost indistinguishable. $D_F^{f/m} = 0.7$ in all models (see Supplementary Data) and $\overline{D}_i^{c/m}$ values are unaltered after H_2O-saturation. If fluid-melt Cl partitioning is non-Nernstian (Supplementary Data), apatite compositional evolution will not follow any single trajectory at set $D_{Cl}^{f/m}$ but will cross between these lines towards higher $D_{Cl}^{f/m}$. Line types illustrate the difference between isobaric (0% H_2O loss; solid lines) H_2O-

saturated crystallisation and polybaric H_2O-saturated crystallisation with 0.1 wt % (dashed lines) and 0.25 wt % H_2O (dotted lines) loss per percent crystallisation.

Figure 9. The effect of varying input parameters in general (i.e. not specific to Campi Flegrei) thermodynamic models of apatite compositional evolution in X_{Cl}/X_{OH} *versus* X_F/X_{OH} (a,c) and X_{Cl}/X_{OH} *versus* X_F/X_{Cl} (b,d) binary space. C_F^0, $\overline{D}_F^{c/m}$, $\overline{D}_{Cl}^{c/m}$, $\overline{D}_{H_2O}^{c/m}$, $D_F^{f/m}$, K_{Cl-F}^{ap-m}, K_{Cl-OH}^{ap-m}, K_{F-OH}^{ap-m} and H_2O speciation are as in Fig. 8d-f. Apatite crystallisation begins at the black point and continues to 85% crystallisation in all models. (a,b) Trajectories of volatile-undersaturated apatite compositional evolution with varying C_i^0. Line colours distinguish models with $C_{H_2O}^0 = 3.0$ wt % (purple), $C_{H_2O}^0 = 1.5$ wt % (green) and $C_{H_2O}^0 = 0.5$ wt % (red). Line types distinguish models with $C_{Cl}^0 = 0.4$ wt % (solid lines) and $C_{Cl}^0 = 0.25$ wt % (dashed lines). (c,d) Trajectories of apatite compositional evolution with varying $C_{H_2O}^{sat}$. C_{Cl}^0 and $C_{H_2O}^0$ are as in Fig. 8 and $D_{Cl}^{f/m} = 20$. The black arrows show an arbitrary trajectory of 61% volatile-undersaturated crystallisation, as in Fig. 8e, f. Line colours show H_2O-saturated crystallisation after 61%, 47% and 28% crystallisation, where $C_{H_2O}^{sat}$ is 7.5 wt % (purple), 5.5 wt % (green) and 4 wt % (red), respectively.

Figure 10. Effect of re-equilibration on apatite compositions during cooling, shown in binary X_{Cl}/X_{OH} *versus* X_F/X_{OH} space. The solid lines represent an arbitrary trend of apatite compositional evolution during volatile-undersaturated (as in Fig. 8b; black line) followed by isobaric H_2O-saturated (as in Fig. 8e; red line) fractional crystallisation. The dotted red line illustrates polybaric H_2O-saturated fractional crystallisation (as in Fig. 8e). The dashed arrows show modelled trajectories of re-equilibration during cooling from 1000 °C to 750 °C, starting from different points on the volatile-undersaturated (point A) and H_2O-saturated (points B-D) trend. In each cooling model, the melt composition is fixed and K_D values are calculated from the *P*-independent regressions of Riker *et al.* (in press). Cooling of a volatile-

undersaturated system, where Cl is retained within the melt (i.e. starting at point A), will cause apatite re-equilibration towards elevated X_{Cl}/X_{OH} and X_F/X_{OH} ratios (black dashed arrow). Extraction of Cl from the melt into the fluid following H_2O-saturation (i.e. starting sequentially from point B to point D) increasingly prevents elevation of X_{Cl}/X_{OH} and drives apatite compositions to high X_F/X_{OH} ratios only (dashed grey lines). Re-equilibration of apatites that grew under volatile-undersaturated conditions to H_2O-saturated conditions could potentially result in intermediate compositions in the space between A-B and B-D.

Figure 11. Schematic diagram summarising volatile systematics in the Campi Flegrei sub-volcanic plumbing system, based on apatite and glass compositions. The representative graphs (right) illustrate how apatite compositional trends relate to different parts of the magmatic system (black lines show apatite trends that form at a particular depth, grey lines show trends that form at a greater depth but are bought up to shallower levels by ascending magmas). The grey bars (left) display relative estimates of Campi Flegrei magma storage depths, derived from independent constraints: 'current unrest' estimates are from recent ground deformation (Amoruso *et al.*, 2014b; D'Auria *et al.*, 2015; Woo & Kilburn, 2010), fumarolic gas emissions (Carlino *et al.*, 2015) and heat flow measurements (Di Maio *et al.*, 2015); melt inclusion estimates are for <15 kyr eruptions and are from 1 – Fourmentraux *et al.* (2012), 2 – Vetere *et al.* (2011), 3 – Arienzo *et al.* (2016) and 4 – Arienzo *et al.* (2010); phase equilibria constraints are from Fowler *et al.* (2007), Bohrson *et al.* (2006) and Cannatelli (2012); seismic tomography data are from Zollo *et al.* (2008) and De Siena *et al.* (2010). Pressure estimates were converted to depths using a consistent crustal density of 2.3 kg/cm^3 after Rosi & Sbrana (1987). Not to scale.

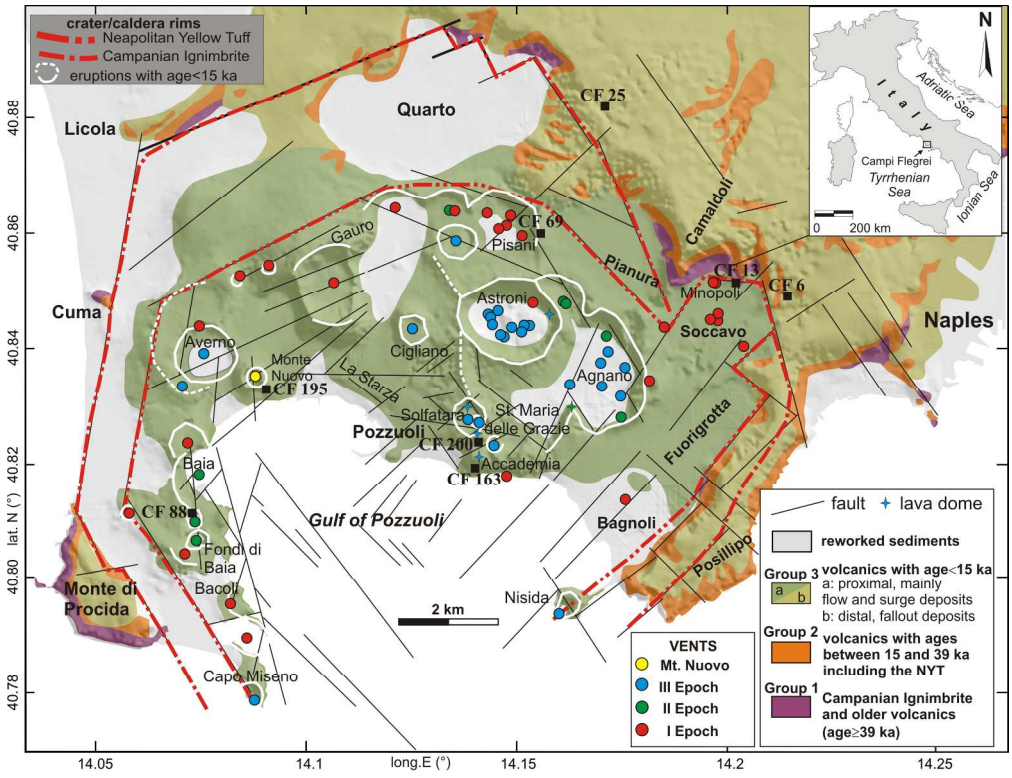

Figure 1. Simplified geological map of the Campi Flegrei caldera showing major structural features, adapted from Vitale and Isaia (2014). The locations of sampling sites (black squares) and vents for each eruption analysed in this study (Table 1) are marked and labelled.

197x150mm (300 x 300 DPI)

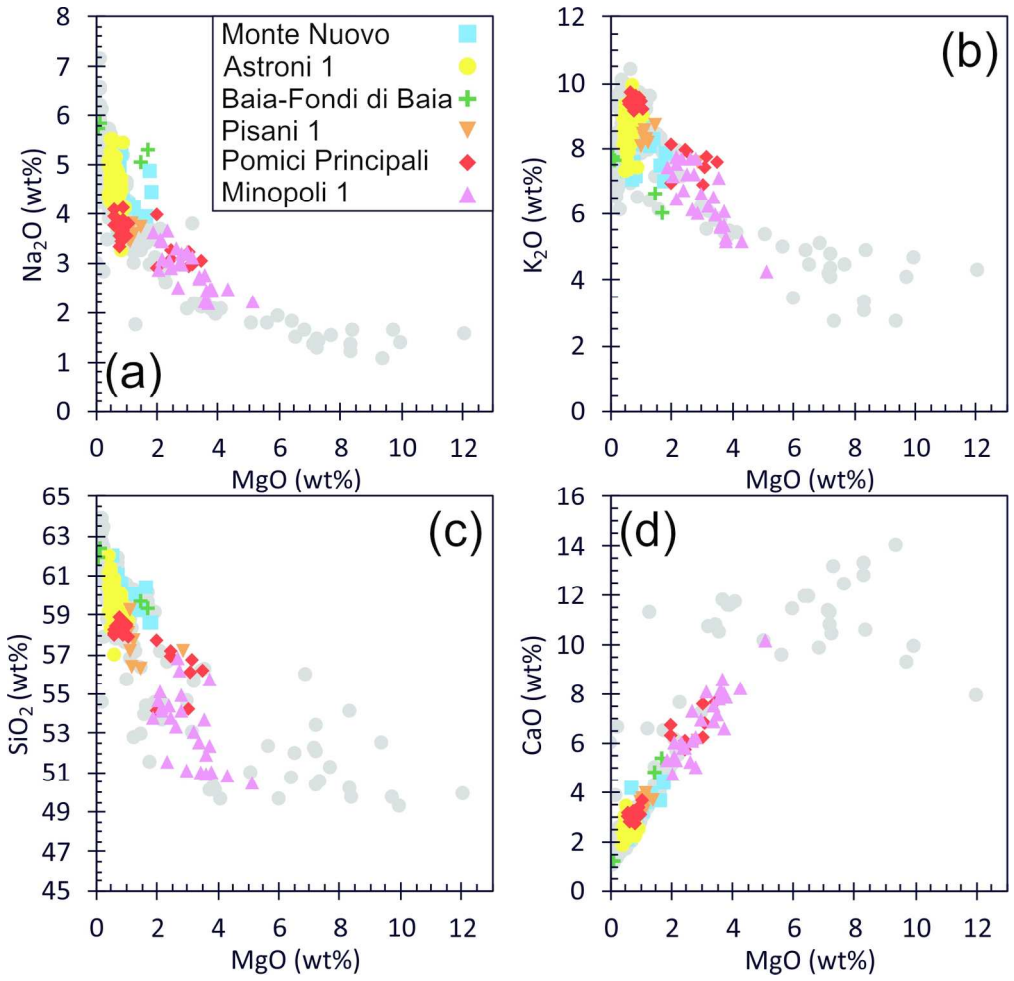

Figure 2. Clinopyroxene-hosted melt inclusion major element compositions from explosive Campi Flegrei eruptions. All data were measured by EPMA and are normalised to 100%. Data are distinguished by eruption (see legend). Grey points show a compilation of literature clinopyroxene- and olivine-hosted melt inclusion compositions in <15 kyr Campi Flegrei deposits, from Cannatelli et al. (2007), Mangiacapra et al. (2008), Arienzo et al. (2010), Arienzo et al. (2016) and Fourmentraux et al. (2012).

177x172mm (300 x 300 DPI)

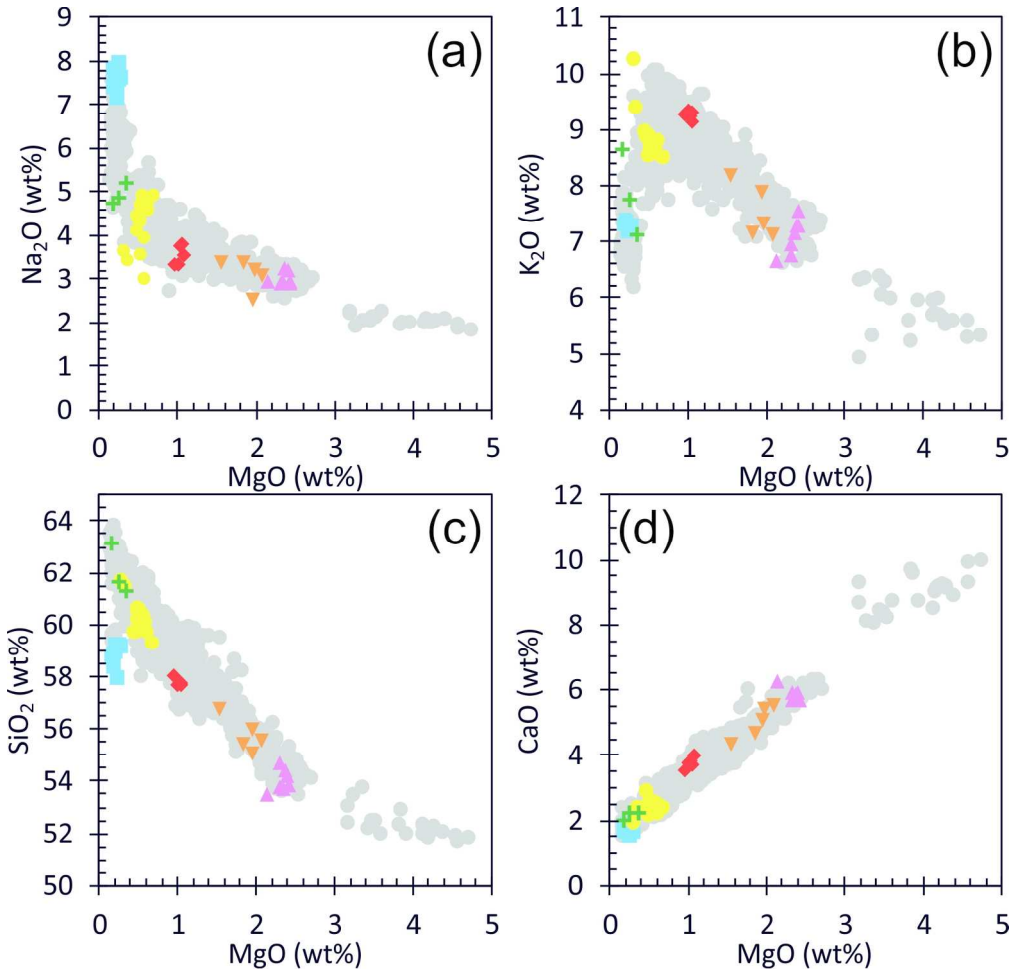

Figure 3. Matrix glass major element compositions from explosive Campi Flegrei eruptions. All data were measured by EPMA and are normalised to 100%. Data are distinguished by eruption (see legend in Fig. 2). Grey points show literature matrix glass compositions in <15 kyr Campi Flegrei deposits, from Smith et al. (2011).

179x172mm (300 x 300 DPI)

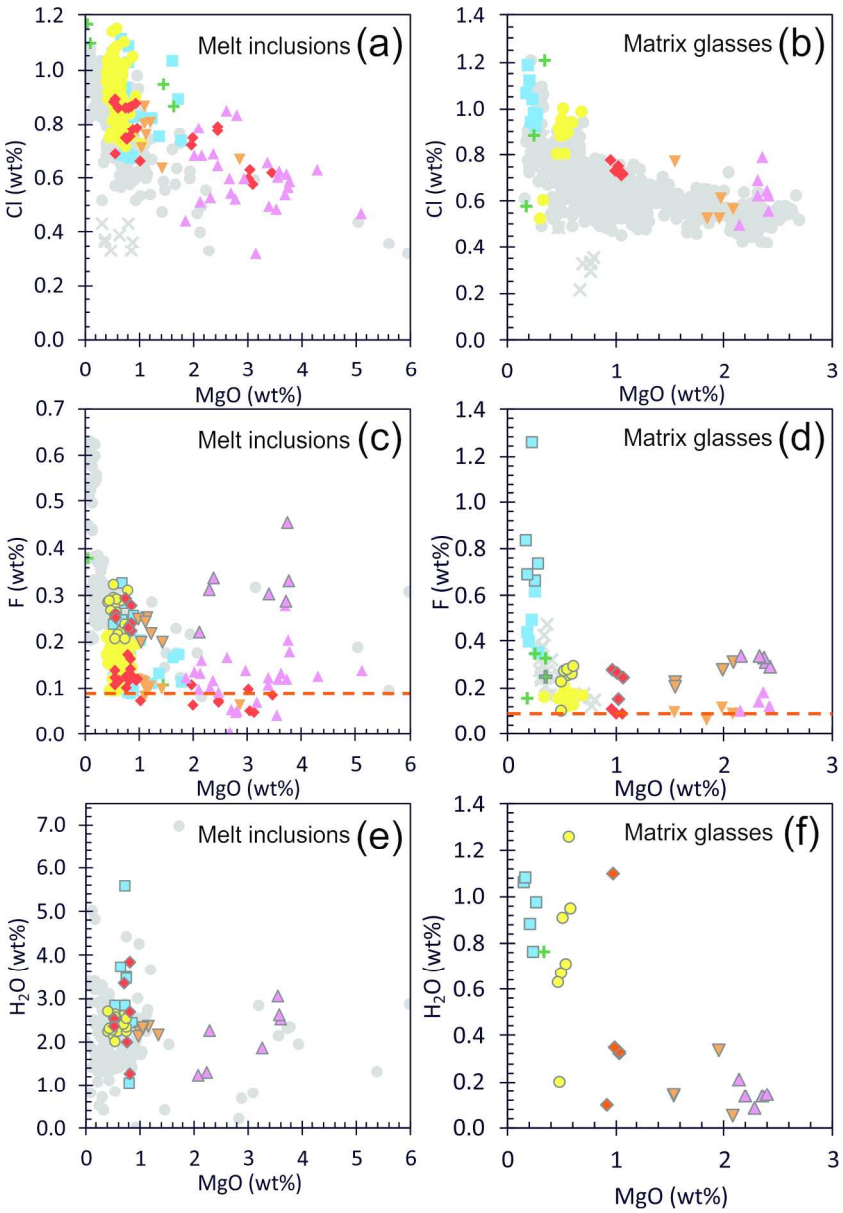

Figure 4. Halogens (a-d) and H_2O (e,f) versus MgO compositions in melt inclusions (a,c,e) and matrix glasses (b,d,f) from explosive Campi Flegrei eruptions. MgO and Cl were measured by EPMA (points with no outlines). F and H_2O were measured by SIMS (points with grey outlines). The red dashed lines show EPMA F detection limits of 0.09 wt%. Data in panels a-d are normalised to 100%. Data are distinguished by eruption (see legend in Fig. 2). Grey circles show literature melt inclusion and matrix glass compositions in <15 kyr Campi Flegrei deposits, from the same sources as Figures 2 and 3, respectively. The grey crosses show the compositions of Campanian Ignimbrite melt inclusions and matrix glasses, from Signorelli et al. (1999).

180x260mm (300 x 300 DPI)

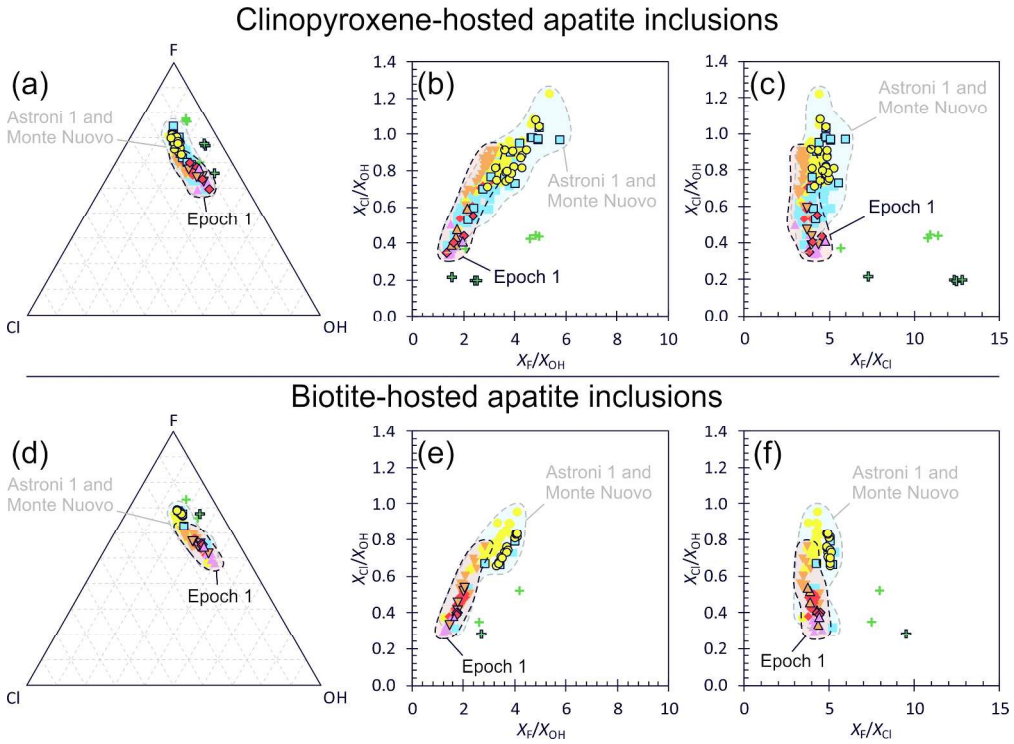

Figure 5. Volatile compositions of clinopyroxene- (a-c) and biotite-hosted (d-f) apatite inclusions from explosive Campi Flegrei eruptions. Data are presented both in ternary space (a,d) and on binary plots of XCl/XOH versus XF/XOH (b,e) and XCl/XOH versus XF/XCl (c,f). Points with black outlines were measured by SIMS and points without outlines were measured by EPMA. Data are distinguished by eruption (see legend in Fig. 2). The coloured fields highlight EPMA and SIMS data from Epoch 1 (red), and Astroni 1 (Epoch 3) and the historic Monte Nuovo eruptions (blue).

276x201mm (300 x 300 DPI)

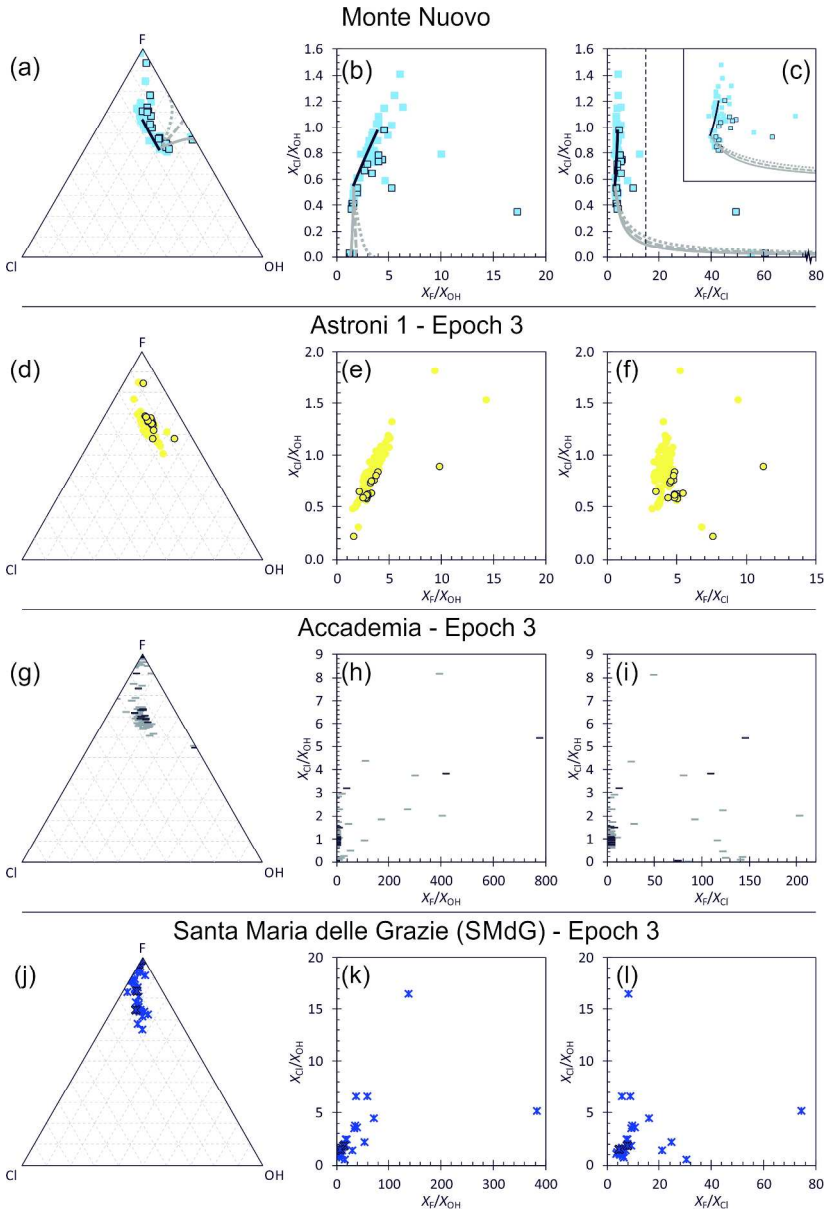

Figure 6. Volatile compositions of apatite microphenocrysts from the historic Monte Nuovo (a-c) and Epoch 3 (d-l) eruptions of Campi Flegrei. Data are presented both in ternary space (a,d,g,j) and on binary plots of XCl/XOH versus XF/XOH (b,e,h,k) and XCl/XOH versus XF/XCl (c,f,i,l). Inset in c shows an expansion of the area outlined by the black dashed box in the main panel. Points with black outlines were measured by SIMS and points without outlines were measured by EPMA. Non-stoichiometric analyses with F >3.76 wt% (i.e. in lava deposits) are plotted as end-member fluorapatite, with non-stoichiometry likely due to F migration during EPMA (Goldoff et al., 2012, Stock et al., 2015, Stormer et al., 1993). Data are distinguished by eruption (see headings). Lines in a-c show the theoretical trajectory of apatite compositional evolution predicted by our thermodynamic model that best fits natural apatite compositions from Campi Flegrei. C_Cl^0= 0.4 wt%, C_F^0= 0.2 wt%, C_(H_2O)^0= 2.5 wt%, K_(Cl-F)^(ap-m)=0.22, K_(Cl-OH)^(ap-m)= 25, K_(F-OH)^(ap-m)= 75, $\bar{D}$_F^(c/m)= 0.99, $\bar{D}$_Cl^(c/m)= 0.8 and $\bar{D}$_(H_2O)^(c/m)= 0.01. H_2O speciation is calculated after Zhang (1999) for temperature of 1020 °C. The black solid line shows modelled apatite compositional evolution during ~70% volatile-undersaturated crystallisation. The grey lines shows

modelled apatite compositional evolution during subsequent H_2O-saturated crystallisation, with D_Cl^(f/m)= 20 and D_Cl^(f/m)= 0.7, after C_(H_2O)^m concentration reaches C_(H_2O)^sat at 7.5 wt%. The grey line types illustrate the difference between isobaric (0% H2O loss; solid lines) H_2O-saturated crystallisation and polybaric H_2O-saturated crystallisation with 0.15 wt% (dashed lines) and 0.25 wt% (dotted lines) H_2O loss from the melt into the fluid phase per percent crystallisation.

276x405mm (300 x 300 DPI)

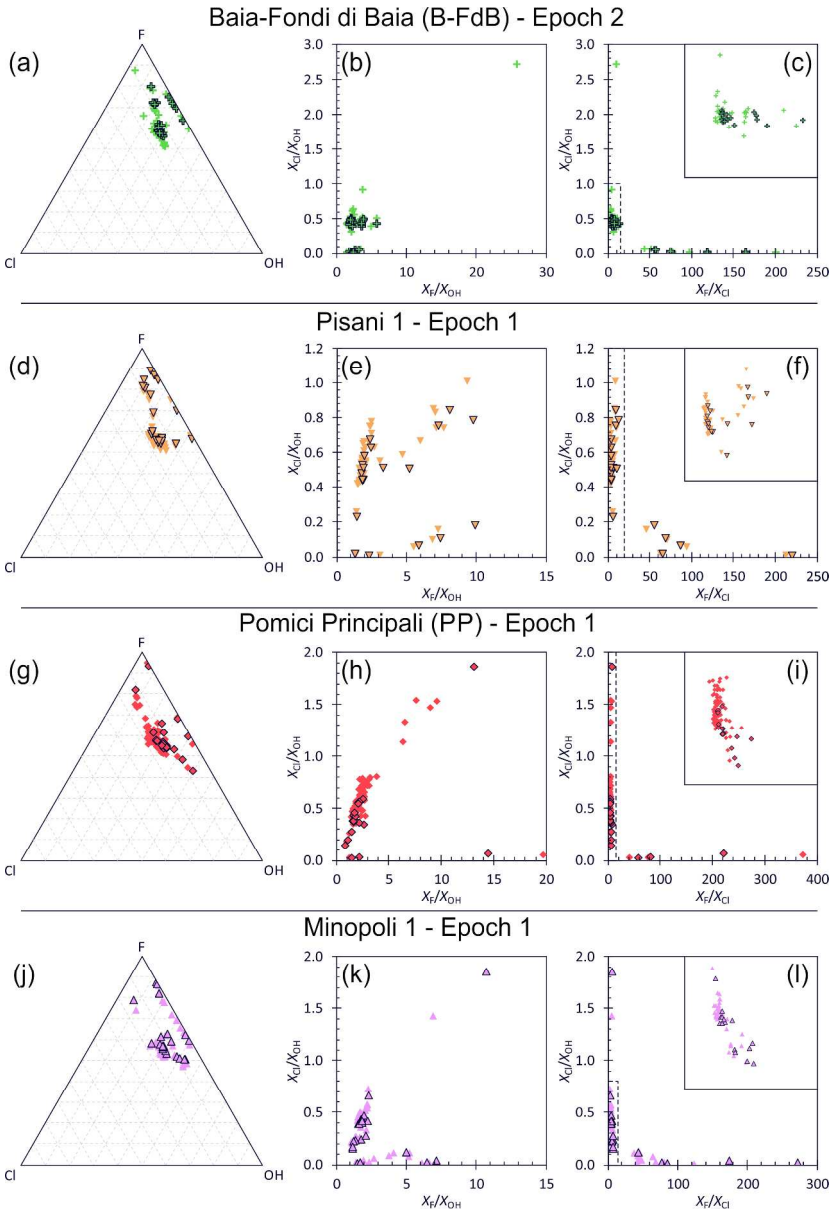

Figure 7. Volatile compositions of apatite microphenocrysts from Epoch 2 (Baia-Fondi di Baia; a-c) and Epoch 1 (d-l) Campi Flegrei eruptions. Data are presented both in ternary space (a,d,g,j) and on binary plots of XCl/XOH versus XF/XOH (b,e,h,k) and XCl/XOH versus XF/XCl (c,f,i,l). Insets in c, f, i and l show expansions of the areas outlined by the black dashed boxes in the main panels. Points with black outlines were measured by SIMS and points without outlines were measured by EPMA. Data are distinguished by eruption (see headings).

277x403mm (300 x 300 DPI)

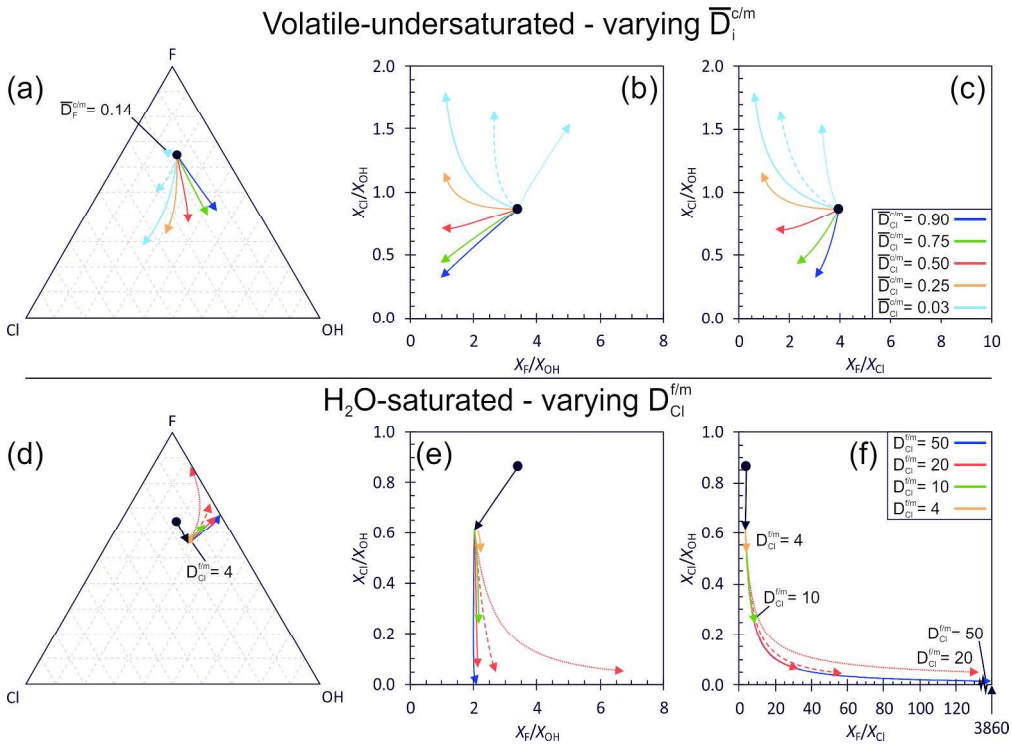

Figure 8. Theoretical apatite compositional trajectories for different crystallisation scenarios (not specific to Campi Flegrei). Data are presented both in ternary (a,d) space and on binary plots of XCl/XOH versus XF/XOH (b,e) and XCl/XOH versus XF/XCl (c,f). In all models, C_Cl^0= 0.4 wt%, C_F^0= 0.2 wt%, C_(H_2O)^0= 2.9 wt%, K_(Cl-F)^(ap-m)=0.22, K_(Cl-OH)^(ap-m)= 25, K_(F-OH)^(ap-m)= 75 and apatite crystallisation begins at the black point (see discussion of input parameters in text). H_2O speciation is calculated after Zhang (1999) for temperature of 1020 °C. (a-c) Apatite compositional evolution during volatile-undersaturated fractional crystallisation. Crystal compositions evolve in the arrow direction until 85% crystallisation. Curves show the effect of varying $\overline{D}$_i^(c/m), where $\overline{D}$_F^(c/m)>$\overline{D}$_Cl^(c/m)>$\overline{D}$_(H_2O)^(c/m) and 1>$\overline{D}$_i^(c/m)>0. Line colours distinguish models with different $\overline{D}$_Cl^(c/m) values (see legend in c). Line types distinguishes models with $\overline{D}$_F^(c/m)=0.99 (solid lines), $\overline{D}$_F^(c/m)=0.5 (dashed lines) and $\overline{D}$_F^(c/m)=0.14 (dotted lines). $\overline{D}$_(H_2O)^(c/m) is set at 0.003; varying $\overline{D}$_(H_2O)^(c/m) affects crystal XF/XOH and XCl/XOH evolution in the opposing sense to $\overline{D}$_F^(c/m)and $\overline{D}$_Cl^(c/m). (d-f) Apatite compositional evolution during H_2O-saturated fractional crystallisation. The black arrow shows an arbitrary trajectory of apatite compositional evolution under volatile-undersaturated conditions ($\overline{D}$_F^(c/m)=0.8, $\overline{D}$_Cl^(c/m)=0.65, $\overline{D}$_(H_2O)^(c/m)=0.001), until 61% crystallisation. Water saturates at 61% crystallisation when C_(H_2O)^m= C_(H_2O)^s=7.5 wt% (see Supplementary Information) and crystal compositions continue to evolve in the arrow direction to 85% crystallisation. Line colours distinguish H_2O-saturated models with varying D_Cl^(f/m) within a realistic range (see legend in f). D_Cl^(f/m)=4 equates to the lowest value measured for phonolitic systems at 150 MPa by Signorelli and Carroll (2000) and apatite trajectories at D_Cl^(f/m)>50 are almost indistinguishable. D_F^(f/m)=0.7 in all models (see Supplementary Information) and $\overline{D}$_i^(c/m) values are unaltered after H_2O-saturation. If fluid-melt Cl partitioning is non-Nernstian (Supplementary Information), apatite compositional evolution will not follow any single trajectory at set D_Cl^(f/m) but will cross between these lines towards higher D_Cl^(f/m). Line types illustrate the difference between isobaric (0% H_2O loss; solid lines) H_2O-saturated crystallisation and polybaric H_2O-saturated crystallisation with 0.1 wt% (dashed lines) and 0.25 wt% H_2O loss (dotted lines) per percent crystallisation.

278x204mm (300 x 300 DPI)

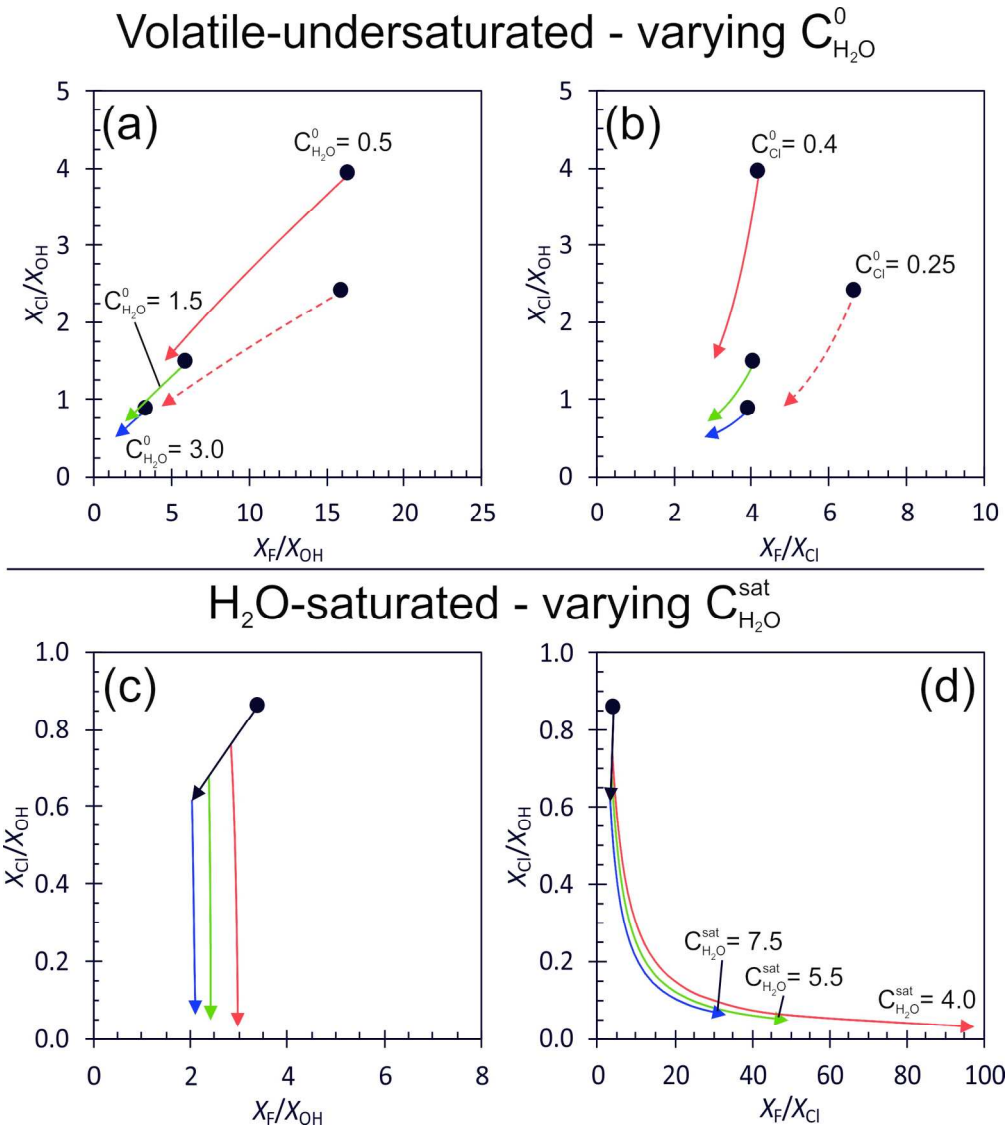

Figure 9. The effect of varying input parameters in general (i.e. not specific to Campi Flegrei) thermodynamic models of apatite compositional evolution in XCl/XOH versus XF/XOH (a,c) and XCl/XOH versus XF/XCl (b,d) binary space. C_F^0, D¯_F^(c/m), D¯_Cl^(c/m), D¯_(H₂O)^(c/m), D_F^(f/m), K_(Cl-F)^(ap-m), K_(Cl-OH)^(ap-m), K_(F-OH)^(ap-m) and H_2O speciation are as in Fig. 8d-f. Apatite crystallisation begins at the black point and continues to 85% crystallisation in all models. (a,b) Trajectories of volatile-undersaturated apatite compositional evolution with varying C_i^0. Line colours distinguish models with C_(H₂O)^0=3.0 wt% (purple), C_(H₂O)^0=1.5 wt% (green) and C_(H₂O)^0=0.5 wt% (red). Line types distinguish models with C_Cl^0=0.4 wt% (solid lines) and C_Cl^0=0.25 wt% (dashed lines). (c,d) Trajectories of apatite compositional evolution with varying C_(H₂O)^sat. C_Cl^0 and C_(H₂O)^0 are as in Figure 8 and D_Cl^(f/m)=20. The black arrows show an arbitrary trajectory of 61% volatile-undersaturated crystallisation, as in Figure 8e,f. Line colours show H_2O-saturated crystallisation after 61%, 47% and 28% crystallisation, where C_(H₂O)^sat is 7.5 wt% (purple), 5.5 wt% (green) and 4 wt% (red), respectively.

182x203mm (300 x 300 DPI)

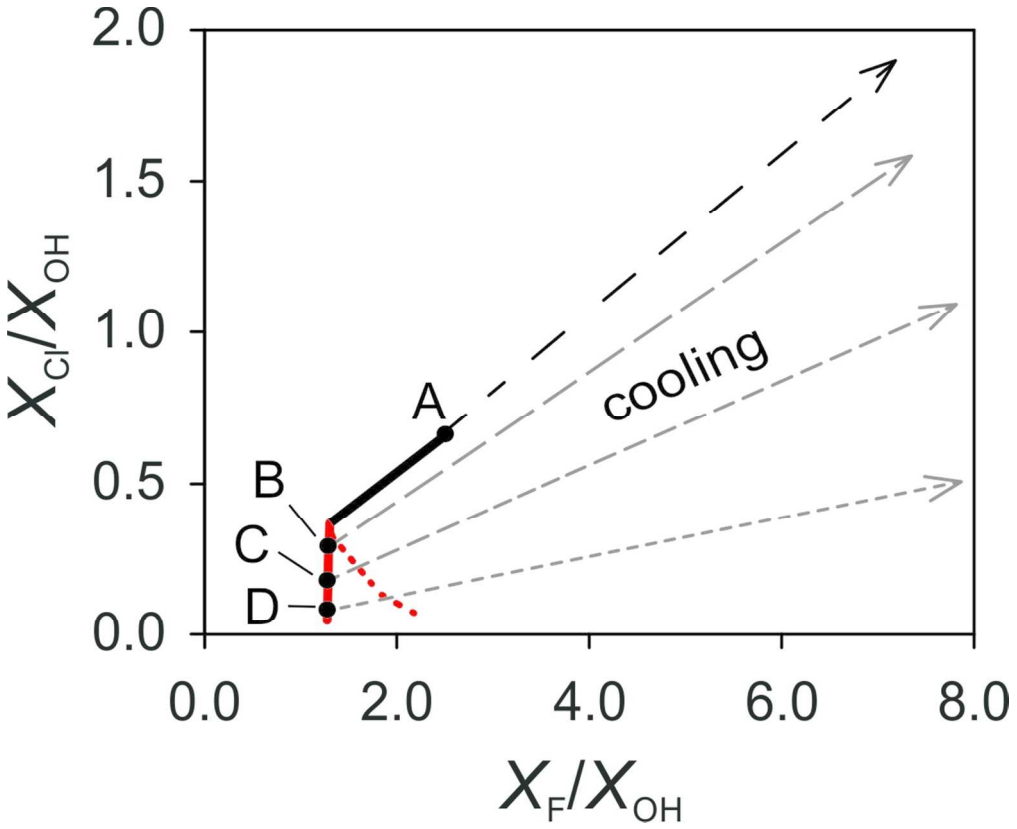

Figure 10. Effect of re-equilibration on apatite compositions during cooling, shown in binary XCl/XOH versus XF/XOH space. The solid lines represent an arbitrary trend of apatite compositional evolution during volatile-undersaturated (as in Fig. 8b; black line) followed by isobaric H_2O-saturated (as in Fig. 8e; red line) fractional crystallisation. The dotted red line illustrates polybaric H_2O-saturated fractional crystallisation (as in Fig. 8e). The dashed arrows show modelled trajectories of re-equilibration during cooling from 1000 °C to 750 °C, starting from different points on the volatile-undersaturated (point A) and H_2O-saturated (points B-D) trend. In each cooling model, the melt composition is fixed and KD values are calculated from the P-independent regressions of Riker et al. (in press). Cooling of a volatile-undersaturated system, where Cl is retained within the melt (i.e. starting at point A), will cause apatite re-equilibration towards elevated XCl/XOH and XF/XOH ratios (black dashed arrow). Extraction of Cl from the melt into the fluid following $_2O$-saturation (i.e. starting sequentially from point B to point D) increasingly prevents elevation of XCl/XOH and drives apatite compositions to high XF/XOH ratios only (dashed grey lines). Re-equilibration of apatites that grew under volatile-undersaturated conditions to H_2O-saturated conditions could potentially result in intermediate compositions in the space between A-B and B-D.

104x85mm (300 x 300 DPI)

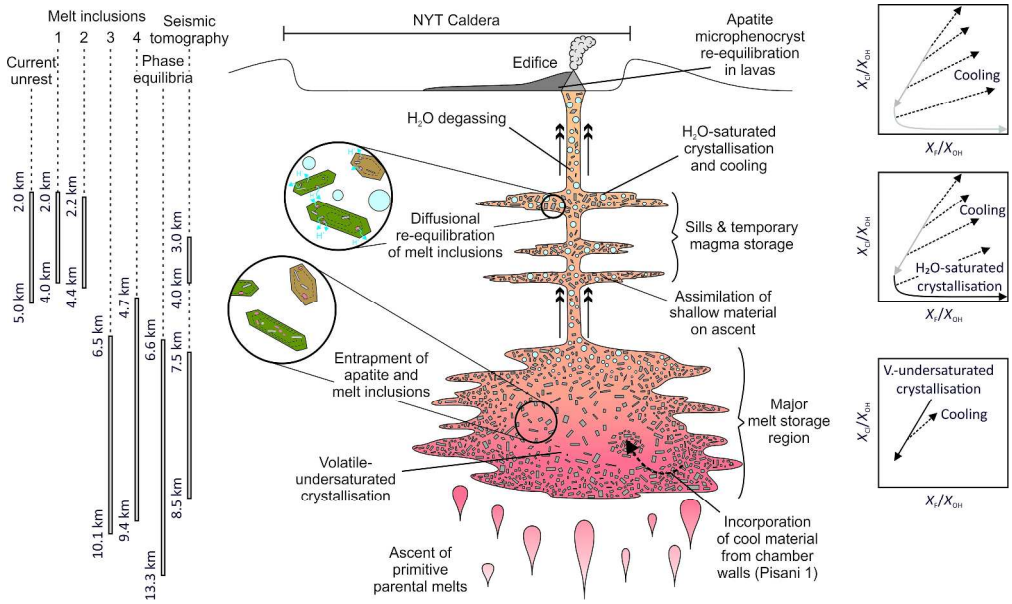

Figure 11. Schematic diagram summarising volatile systematics in the Campi Flegrei sub-volcanic plumbing system, based on apatite and glass compositions. The representative graphs (right) illustrate how apatite compositional trends relate to different parts of the magmatic system (black lines show apatite trends that form at a particular depth, grey lines show trends that form at a greater depth but are bought up to shallower levels by ascending magmas). The grey bars (left) display relative estimates of Campi Flegrei magma storage depths, derived from independent constraints: 'current unrest' estimates are from recent ground deformation (Amoruso et al., 2014b, D'Auria et al., 2015, Woo & Kilburn, 2010), fumarolic gas emissions (Carlino et al., 2015) and heat flow measurements (Di Maio et al., 2015); melt inclusion estimates are for <15 kyr eruptions and are from 1 – Fourmentraux et al. (2012), 2 – Vetere et al. (2011), 3 – Arienzo et al. (2016) and 4 – Arienzo et al. (2010); phase equilibria constraints are from Fowler et al. (2007), Bohrson et al. (2006) and Cannatelli (2012); seismic tomography data are from Zollo et al. (2008) and De Siena et al. (2010). Pressure estimates were converted to depths using a consistent crustal density of 2.3 kg/cm3 after Rosi and Sbrana (1987). Not to scale.

378x224mm (300 x 300 DPI)

Epoch	Eruption	Sample number	Age (yr)	Deposit type	Erupted volume (km^3)	Average matrix glass composition	Vent location*		Sampling location	
							UTM X	UTM Y	UTM X	UTM Y
	Monte Nuovo	CF195	479*	Pyroclastic density current deposit	~0.03*	Phonolite	423095	4520870	423277	4520614
Epoch 3	Astroni 1	CF69	4155-4357*	Ash fall with some lapilli layers	~0.06*	Phonolite	427999	4522122	428859*	4523584*
	Accademia	CF163	4205-4507*[a]	Lava dome	<0.01*	Trachyte[§]	427551	4519282	427597	4519562
	Santa Maria delle Grazie	CF200	4383-4507*	Shallow feeder dyke	<0.01*	Latite[‖]	427625	4519806	427421	4518909
Epoch 2	Baia-Fondi di Baia	CF88	9525-9705*	Pumice fall	0.02-0.04[†]	Trachyte	421855	4517930	421844*	4518253*
Epoch 1	Pisani 1	CF25	10516-12107*[b]	Scoria fall	0.1-0.3*	Tephri-phonolite – trachy-andesite	428260	4523970	430237*	4525994*
	Pomici Principali	CF6	11907-12107*	Plinian fall (B3 unit)	0.43-1.28[‡]	Tephri-phonolite – phonolite	428698	4522284	433890*	4522346*
	Minopoli 1	CF13	11907-12725*[c]	Scoria fall	<0.1*	Phono-tephrite – tephri-phonolite	432400	4522670	432805*	4522632*

Table 1. Summary of eruption deposits analysed, including age estimate, deposit characteristics (i.e. eruption style), erupted volume (i.e. magnitude estimate), average matrix glass composition, vent location and sampling location. Erupted volumes are dense rock equivalent. Where exposure permitted, samples were collected vertically through volcaniclastic units and included both lapilli- and ash-sized material. The Pomici Principali sample represents only the B3 Plinian phase of the eruption and the Baia-Fondi di Baia sample comprises only the basal Baia fallout units. Samples of these deposits only show limited compositional diversity (Smith *et al.*, 2011) and the samples are therefore assumed representative of the bulk erupted material.

* Data from Smith *et al.* (2011). All ages of Smith *et al.* (2011) have been recalibrated using IntCal13 (Reimer *et al.*, 2013).
† Data from Pistolesi *et al.* (2017).
‡ Data from Bevilacqua *et al.* (2016).
§ Bulk rock composition from Melluso *et al.* (2012).
‖ Bulk rock composition from Isaia *et al.* (2009).
[a] Eruption not dated precisely but stratigraphically older than the Solfatara eruption (4205-4427 yr) and younger than Santa Maria delle Grazie.
[b] Eruption not dated precisely but stratigraphically older than Pisani 3 (10517-10760 yr) and younger than Pomici Principali.
[c] Eruption not dated precisely but stratigraphically older than Pomici Principali and younger than Archiaverno (12579-12725 yr).

Eruption	Monte Nuovo	Monte Nuovo	Monte Nuovo	Monte Nuovo	Monte Nuovo	Monte Nuovo	Monte Nuovo	Monte Nuovo	Monte Nuovo	Monte Nuovo
Analysis #	CF195_cpx113_m6	CF195_cpx64_m1	CF195_cpx86_m2	CF195_cpx86_m3	CF195_cpx110_m1	CF195_cpx113_m7	CF195_cpx122_m1	CF195_cpx122_m2	CF195_cpx123_m3	CF195_cpx137_m5
Type	mi	mi	mi	mi	mi	mi	mi	mi	mi	mi
SiO_2	58.77	57.35	57.81	56.19	58.05	57.63	58.35	58.26	59.68	58.71
Na_2O	4.45	4.04	4.11	3.94	5.04	4.65	4.20	4.08	5.03	4.42
MgO	0.55	0.77	0.75	0.74	0.76	0.59	0.87	0.81	0.51	0.70
Al_2O_3	18.17	17.70	18.27	17.26	16.54	18.02	18.03	18.12	16.97	17.71
K_2O	8.40	8.57	8.49	7.89	6.86	8.37	8.48	8.94	7.43	8.42
CaO	2.22	2.59	2.55	2.48	2.72	2.26	2.81	2.83	2.33	2.24
TiO_2	0.43	0.48	0.48	0.42	0.55	0.46	0.50	0.44	0.53	0.49
MnO	0.09	0.09	0.11	0.15	0.19	0.08	0.10	0.12	0.12	0.11
FeOt	3.31	3.82	3.46	3.39	3.96	3.38	3.83	3.66	3.85	3.37
P_2O_5	0.08	0.15	0.13	0.14	0.08	0.12	0.13	0.13	0.10	0.11
Cl	0.95	0.66	0.73	0.64	0.85	0.84	0.67	0.66	0.94	0.77
F	0.25	0.22	0.23	0.22	0.22	0.28	0.25	0.22	0.23	0.28
H_2O	2.82	3.48	2.84	5.56	3.47	2.45	2.44	1.04	2.28	2.54
Total	100.47	99.93	99.96	99.01	99.29	99.12	100.67	99.31	100.01	99.87

Eruption	Monte Nuovo	Monte Nuovo	Monte Nuovo	Monte Nuovo	Monte Nuovo	Monte Nuovo	Monte Nuovo	Astroni 1	Astroni 1	Astroni 1
Analysis #	CF195_cpx159_m4	CF195_cpx188_m1	VF55_cf195_1_1	VF55_cf195_2_1	VF55_cf195_3_1	VF55_cf195_4_1	VF55_cf195_4_2	CF69_cpx22_m1	CF69_cpx23_m2	CF69_cpx55_m1
Type	mi	mi	mg	mg	mg	mg	mg	mi	mi	mi
SiO_2	57.83	58.59	56.50	57.19	58.62	57.66	57.48	57.70	59.17	56.74
Na_2O	4.85	4.77	6.88	7.88	7.56	7.69	7.29	4.39	4.25	4.26
MgO	0.66	0.68	0.21	0.25	0.28	0.17	0.18	0.65	0.42	0.54
Al_2O_3	17.10	17.52	18.28	18.79	19.04	18.69	18.87	17.90	17.84	18.07
K_2O	7.18	8.25	6.88	7.23	7.25	7.20	7.30	8.08	8.36	8.89
CaO	2.59	2.52	1.81	1.51	1.66	1.69	1.75	2.47	2.19	2.17
TiO_2	0.50	0.47	0.49	0.50	0.39	0.45	0.43	0.45	0.49	0.41
MnO	0.20	0.13	0.24	0.37	0.20	0.20	0.28	0.10	0.19	0.04
FeOt	3.91	3.38	3.08	3.30	2.74	2.89	3.19	3.36	3.65	3.15
P_2O_5	0.15	0.11	0.01	0.00	0.00	0.05	0.07	0.12	0.10	0.08
Cl	0.89	0.78	0.90	0.97	0.97	1.05	1.17	0.96	1.00	0.87
F	0.24	0.32	1.21	0.65	0.73	0.82	0.68	0.28	0.28	0.26
H_2O	3.71	2.38	0.88	0.76	0.97	1.06	1.08	2.37	2.22	2.12
Total	99.80	99.88	97.36	99.41	100.41	99.60	99.77	98.82	100.15	97.60

Eruption	Astroni 1	Astroni 1	Astroni 1	Astroni 1	Astroni 1	Astroni 1	Astroni 1	Astroni 1	Astroni 1	Astroni 1
Analysis #	CF69_cpx55_m2	CF69_cpx66_m1	CF69_cpx66_m3	CF69_cpx82_m1	CF69_cpx91_m1	CF69_cpx92_m1	CF69_cpx97_m3	CF69_cpx113_m1	CF69_cpx116_m1	CF69_cpx127_m1
Type	mi	mi	mi	mi	mi	mi	mi	mi	mi	mi
SiO_2	56.99	54.97	56.56	56.78	58.21	57.38	57.73	56.74	56.44	56.55
Na_2O	4.52	4.15	4.02	4.20	4.60	4.35	4.46	4.76	3.65	4.22
MgO	0.53	0.61	0.72	0.50	0.51	0.76	0.54	0.55	0.78	0.58
Al_2O_3	17.82	17.60	18.24	17.90	17.67	18.60	17.91	17.51	18.40	17.65
K_2O	8.50	8.55	8.83	8.35	8.37	8.44	8.27	8.57	8.84	8.28
CaO	2.15	2.43	2.62	2.07	2.03	2.47	2.34	2.17	2.37	2.34
TiO_2	0.44	0.47	0.47	0.45	0.48	0.41	0.45	0.45	0.51	0.45
MnO	0.13	0.09	0.12	0.19	0.20	0.11	0.12	0.15	0.02	0.10
FeOt	3.37	3.76	4.20	3.40	3.40	2.85	3.38	3.19	3.27	3.84
P_2O_5	0.10	0.14	0.13	0.13	0.08	0.17	0.08	0.08	0.15	0.15
Cl	0.93	0.75	0.69	0.91	1.03	0.84	0.90	0.93	0.73	0.82
F	0.25	0.21	0.23	0.28	0.31	0.30	0.25	0.25	0.22	0.20
H_2O	2.56	2.21	2.58	2.29	2.27	2.21	2.00	2.62	2.33	2.51
Total	98.28	95.94	99.41	97.46	99.16	98.90	98.43	97.97	97.71	97.70

Eruption	Astroni 1	Astroni 1	Astroni 1	Astroni 1	Astroni 1	Astroni 1	Astroni 1	Astroni 1	Astroni 1	Astroni 1
Analysis #	CF69_cpx127_m3	CF69_cpx130_m1	CF69_cpx138_m2	CF69_cpx156_m2	CF69_cpx182_m1	CF69_cpx182_m2	VF55_cf69_2_1	VF55_cf69_3_1	VF55_cf69_5_1	VF55_cf69_6_1
Type	mi	mi	mi	mi	mi	mi	mg	mg	mg	mg
SiO_2	57.17	56.80	55.39	58.52	55.35	55.59	59.14	57.69	59.43	58.83
Na_2O	4.07	4.51	4.62	4.56	3.76	3.87	3.90	4.38	4.67	4.50
MgO	0.54	0.55	0.42	0.45	0.71	0.77	0.54	0.50	0.49	0.58
Al_2O_3	17.63	17.67	17.09	17.12	17.52	17.53	18.37	17.85	18.09	18.11
K_2O	8.36	8.37	8.48	8.03	8.53	8.48	8.61	8.47	8.44	8.56
CaO	2.31	2.30	2.01	2.23	2.64	2.70	2.29	2.28	2.45	2.36
TiO_2	0.49	0.51	0.40	0.48	0.48	0.50	0.48	0.42	0.46	0.37
MnO	0.14	0.11	0.13	0.16	0.12	0.17	0.16	0.17	0.16	0.07
FeOt	3.60	3.40	3.34	3.53	3.90	3.39	3.27	3.31	3.42	3.41
P_2O_5	0.16	0.10	0.06	0.09	0.20	0.12	0.04	0.09	0.09	0.05
Cl	0.88	0.93	0.97	0.91	0.74	0.73	0.91	0.91	0.94	0.92
F	0.20	0.28	0.27	0.26	0.19	0.21	0.25	0.26	0.22	0.25
H_2O	2.57	2.43	2.69	2.30	2.39	2.51	0.71	0.67	0.20	1.26
Total	98.12	97.95	95.85	98.63	96.52	96.58	98.67	96.99	99.06	99.27

Eruption	Astroni 1	Astroni 1	Astroni 1	Baia-Fondi di Baia	Pisani 1	Pisani 1	Pisani 1	Pisani 1	Pisani 1	Pisani 1
Analysis #	VF55_cf69_8_1	VF55_cf69_9_1	VF55_cf69_9_2	VF55_cf88_1_2	CF25_cpx86_m3	CF25_cpx129_m3	CF25_cpx54_m3	CF25_cpx118_m3	CF25_cpx129_m1	CF25_cpx129_m2
Type	mg	mg	mg	mg	mi	mi	mi	mi	mi	mi
SiO_2	58.84	56.79	58.68	58.39	52.97	55.86	55.81	52.47	57.52	55.12
Na_2O	4.26	2.87	4.52	4.95	3.53	3.36	3.46	3.55	3.57	3.55
MgO	0.48	0.52	0.59	0.34	1.34	1.00	1.17	1.05	0.97	1.07
Al_2O_3	18.19	18.09	18.01	16.03	17.97	17.53	17.89	17.60	18.25	18.01
K_2O	8.65	8.09	8.67	6.79	8.20	8.14	7.88	7.70	7.98	7.99
CaO	2.10	2.41	2.49	2.14	3.43	3.57	3.58	3.65	3.57	3.58
TiO_2	0.40	0.48	0.45	0.54	0.62	0.59	0.63	0.64	0.58	0.56
MnO	0.18	0.14	0.20	0.26	0.02	0.21	0.10	0.13	0.22	0.22
FeOt	3.06	3.37	3.33	4.29	4.70	4.76	4.91	5.03	5.23	5.07
P_2O_5	0.09	0.10	0.13	0.05	0.45	0.24	0.25	0.28	0.18	0.21
Cl	0.86	0.85	0.92	1.15	0.60	0.69	0.78	0.71	0.77	0.83
F	0.09	0.26	0.29	0.23	0.19	0.19	0.21	0.23	0.24	0.23
H_2O	0.63	0.91	0.95	0.77	2.17	2.23	2.37	2.30	2.12	2.32
Total	97.83	94.89	99.23	95.92	96.17	98.39	99.04	95.35	101.22	98.75

Eruption	Pisani 1	Pisani 1	Pisani 1	Pisani 1	Pomici Principali	Pomici Principali	Pomici Principali	Pomici Principali	Pomici Principali	Pomici Principali
Analysis #	VF55_cf25_2_1a	VF55_cf25_2_1b	VF55_cf25_4_1	VF55_cf25_4_2	CF6_cpx29_m1	CF6_cpx98_m1	CF6_cpx110_m1	CF6_cpx121_m2	CF6_cpx192_m1	CF6_cpx_137_2
Type	mg	mg	mg	mg	mi	mi	mi	mi	mi	mi
SiO_2	56.27	56.27	55.42	54.66	57.09	56.58	56.59	57.57	57.05	56.34
Na_2O	3.34	3.34	3.08	3.17	4.06	3.70	3.83	3.39	3.24	3.95
MgO	1.53	1.53	2.08	1.96	0.82	0.83	0.54	0.77	0.72	0.54
Al_2O_3	17.82	17.82	17.90	18.21	18.24	18.19	18.21	18.45	18.11	18.15
K_2O	8.13	8.13	7.11	7.27	9.28	9.22	9.18	9.08	8.84	9.10
CaO	4.27	4.27	5.52	5.35	3.16	3.18	2.95	3.17	3.14	3.06
TiO_2	0.65	0.65	0.75	0.81	0.41	0.45	0.47	0.48	0.46	0.55
MnO	0.09	0.09	0.13	0.06	0.09	0.16	0.17	0.04	0.14	0.14
FeOt	5.41	5.41	6.21	6.07	3.67	3.92	3.94	3.82	3.89	3.90
P_2O_5	0.42	0.42	0.50	0.49	0.14	0.14	0.17	0.12	0.12	0.11
Cl	0.76	0.76	0.56	0.61	0.74	0.73	0.67	0.73	0.72	0.86
F	0.22	0.20	0.31	0.27	0.23	0.22	0.25	0.22	0.28	0.24
H_2O	0.14	0.14	0.05	0.33	1.26	3.84	2.52	1.98	3.35	2.35
Total	99.06	99.04	99.63	99.26	99.21	101.16	99.47	99.82	100.05	99.30

Eruption	Pomici Principali	Pomici Principali	Pomici Principali	Pomici Principali	Pomici Principali	Pomici Principali	Minopoli 1	Minopoli 1	Minopoli 1	Minopoli 1
Analysis #	CF6_cpx_167_1	VF55_cf6_1_1	VF55_cf6_1_2	VF55_cf6_1_3	VF55_cf6_1_4	VF55_cf6_1_6	CF13_cpx29_m1	CF13_cpx142_m1	CF13_cpx_140_1	CF13_cpx_135_1
Type	mi	mg	mg	mg	mg	mg	mi	mi	mi	mi
SiO_2	56.56	56.31	55.90	56.52	55.79	56.16	49.19	49.92	53.36	54.30
Na_2O	3.54	3.71	3.21	3.25	3.45	3.67	2.61	3.54	2.36	3.44
MgO	0.83	1.03	0.92	0.98	1.03	1.00	3.26	2.23	3.56	2.07
Al_2O_3	18.41	17.98	17.96	18.45	17.74	17.99	18.29	18.30	16.98	18.35
K_2O	9.00	8.90	8.94	9.16	9.00	8.98	5.78	7.45	5.82	7.62
CaO	3.17	3.64	3.43	3.68	3.86	3.69	7.30	5.83	6.35	5.35
TiO_2	0.44	0.45	0.47	0.47	0.50	0.42	0.98	0.86	0.66	0.83
MnO	0.17	0.13	0.19	0.12	0.04	0.17	0.12	0.17	0.11	0.14
FeOt	3.56	4.24	4.13	4.18	4.18	4.24	7.42	7.02	4.85	4.82
P_2O_5	0.15	0.17	0.12	0.16	0.22	0.14	0.66	0.63	0.68	0.63
Cl	0.84	0.69	0.75	0.71	0.69	0.73	0.48	0.51	0.59	0.77
F	0.27	0.24	0.27	0.26	0.24	0.14	0.29	0.30	0.28	0.22
H_2O	2.69	0.32	0.10	1.10	0.33	0.35	1.87	1.30	3.05	1.25
Total	99.63	97.82	96.39	99.03	97.07	97.69	98.25	98.06	98.64	99.80

Eruption	Minopoli 1	Minopoli 1	Minopoli 1	Minopoli 1	Minopoli 1	Minopoli 1	Minopoli 1	Minopoli 1		
Analysis #	CF13_cpx_55_1	CF13_cpx_49_2	CF13_cpx119_m1	VF55_cf13_1_2	VF55_cf13_3_1	VF55_cf13_4_1	VF55_cf13_5_1	VF55_cf13_10_1		RP
Type	mi	mi	mi	mg	mg	mg	mg	mg		
SiO_2	52.65	49.23	48.34	53.43	53.34	49.92	53.38	53.01		0.42
Na_2O	2.96	2.40	2.32	3.15	2.91	3.01	2.96	2.87		0.26
MgO	2.29	3.62	3.57	2.35	2.40	2.19	2.14	2.28		0.06
Al_2O_3	17.30	17.53	17.55	16.79	17.06	15.73	18.49	17.27		0.23
K_2O	6.50	5.09	4.88	7.17	7.47	6.65	6.64	6.67		0.20
CaO	5.63	7.79	7.51	5.82	5.65	5.47	6.27	5.82		0.12
TiO_2	0.92	0.98	0.83	1.04	1.01	0.97	0.92	0.95		0.08
MnO	0.18	0.20	0.18	0.19	0.18	0.13	0.17	0.25		0.09
FeOt	6.90	7.93	7.82	6.98	6.94	6.74	7.02	7.32		0.25
P_2O_5	0.44	0.65	0.70	0.68	0.76	0.59	0.59	0.67		0.02
Cl	0.67	0.55	0.55	0.63	0.55	0.73	0.50	0.62		0.06
F	0.33	0.44	0.31	0.31	0.29	0.30	0.34	0.33		0.01
H_2O	2.26	2.53	2.63	0.14	0.14	0.14	0.21	0.08		0.37
Total	99.03	98.92	97.19	98.69	98.71	92.58	99.61	98.13		

Table 2. Major and volatile element analyses of representative Campi Flegrei glasses. F and H_2O were measured by SIMS, all other elements were measured by EPMA. Analysis type refers to textural association: mi, melt inclusion; mg, matrix glass. Concentrations are in wt%. RP is representative absolute precision with one standard deviation based on counting statistics for F and elements measured by EPMA, and a 95% confidence interval based on regression of calibration standards for H_2O.

Eruption	Monte Nuovo	Monte Nuovo	Monte Nuovo	Monte Nuovo	Monte Nuovo	Monte Nuovo	Monte Nuovo	Monte Nuovo	Monte Nuovo	Monte Nuovo
Crystal #	CFmap2_CF195_19	CFmap2_CF195_16	CFmap2_CF195_17	CFmap2_CF195_8	CFmap2_CF195_49	CFmap2_CF195_38	CFmap2_CF195_35	CFmap2_CF195_30	CFmap2_CF195_24	CFmap2_CF195_22
Type	mpc	mpc	mpc	mpc	mpc	mpc	mpc	mpc	mpc	mpc
P_2O_5	38.91	41.20	41.37	41.38	41.63	40.09	41.37	41.34	40.92	40.93
SiO_2	1.60	0.58	0.40	0.42	0.66	0.85	0.44	0.58	0.55	0.69
CaO	53.97	54.09	54.28	54.00	53.42	52.59	53.49	54.32	53.79	53.28
SO_2	1.34	0.70	0.42	0.41	0.14	0.63	0.42	0.19	0.56	0.44
F	2.30	2.03	2.03	2.13	2.83	2.08	2.09	2.58	2.29	2.56
Cl	0.07	0.92	0.90	0.93	0.88	1.02	0.91	0.86	1.04	0.89
OH	1.57	1.09	1.08	1.20	0.57	1.19	1.13	0.57	0.75	0.66
O≡F,Cl,OH	1.72	1.58	1.57	1.67	1.66	1.67	1.62	1.55	1.55	1.59
Total	98.04	99.03	98.91	98.80	98.47	96.78	98.23	98.89	98.35	97.86

Eruption	Monte Nuovo	Monte Nuovo	Monte Nuovo	Monte Nuovo	Monte Nuovo	Monte Nuovo	Monte Nuovo	Monte Nuovo	Monte Nuovo	Monte Nuovo
Crystal #	CFmap2_CF195_45	CFmap2_CF195_31	CFmap2_CF195_12	CFmap2_CF195_97	CFmap2_CF195_46	CFmap2_CF195_64	CFmap2_CF195_74	CFmap2_CF195_98	CF195_cpx63_ap1	CF195_cpx80_ap4
Type	mpc	mpc	mpc	mpc	mpc	mpc	mpc	mpc	cpx	cpx
P_2O_5	40.97	40.47	41.32	40.99	41.39	41.06	40.36	41.36	41.29	41.35
SiO_2	0.68	1.32	0.61	0.54	0.41	0.43	0.90	0.63	0.61	0.50
CaO	53.20	52.93	53.68	54.32	53.37	54.19	53.78	54.67	53.85	54.13
SO_2	0.25	0.17	0.56	0.23	0.27	0.42	0.13	0.16	0.39	0.36
F	2.28	2.02	2.47	2.36	2.50	2.08	2.94	3.30	2.12	2.35
Cl	1.05	0.94	0.98	1.04	0.89	1.04	0.54	0.12	0.98	0.92
OH	1.02	1.23	0.48	0.70	0.55	0.94	0.49	0.17	0.62	0.45
O≡F,Cl,OH	1.68	1.64	1.49	1.56	1.51	1.55	1.59	1.50	1.41	1.41
Total	97.77	97.44	98.61	98.62	97.87	98.61	97.55	98.91	98.44	98.64

Eruption	Monte Nuovo	Monte Nuovo	Monte Nuovo	Monte Nuovo	Monte Nuovo	Monte Nuovo	Monte Nuovo	Monte Nuovo	Monte Nuovo	Monte Nuovo
Crystal #	CF195_cpx83_ap3	CF195_cpx80_ap1	CF195_cpx128_ap1	CF195_cpx128_ap4	CF195_cpx133_ap1	CF195_cpx137_ap1	CF195_cpx173_ap1	CF195_cpx121_ap1	CF195_cpx188_ap1	CF195_cpx208_ap1
Type	cpx	cpx	cpx	cpx	cpx	cpx	cpx	cpx	cpx	cpx
P_2O_5	41.93	41.30	40.73	41.02	40.57	40.96	39.65	40.21	40.89	40.80
SiO_2	0.37	0.45	0.79	0.72	0.48	0.60	1.32	0.67	0.67	0.76
CaO	53.36	53.87	53.18	53.80	53.63	53.84	53.03	53.76	53.94	54.25
SO_2	0.21	0.36	0.34	0.25	0.57	0.55	0.12	0.49	0.40	0.50
F	2.23	2.35	2.30	2.36	2.07	2.51	2.06	2.52	2.53	2.00
Cl	0.94	0.91	1.00	0.79	0.97	0.92	0.91	0.92	0.79	0.91
OH	0.47	0.45	0.53	0.52	0.67	0.46	0.84	0.46	0.39	0.74
O≡F,Cl,OH	1.37	1.41	1.44	1.42	1.40	1.48	1.46	1.48	1.43	1.39
Total	98.13	98.29	97.42	98.05	97.56	98.35	96.47	97.54	98.19	98.57

Eruption	Monte Nuovo	Monte Nuovo	Monte Nuovo	Monte Nuovo	Astroni 1	Astroni 1	Astroni 1	Astroni 1	Astroni 1	Astroni 1
Crystal #	CF195_cpx250_ap4	CF195_bt40_ap1	CF195_bt46_ap1	CF195_bt64_ap3	CFmap2_CF69_47	CFmap2_CF69_32	CFmap2_CF69_29	CFmap2_CF69_10	CFmap2_CF69_26	CFmap2_CF69_6
Type	cpx	bt	bt	bt	mpc	mpc	mpc	mpc	mpc	mpc
P_2O_5	38.59	40.83	39.77	41.62	41.50	40.85	42.62	41.65	41.26	41.40
SiO_2	1.46	0.80	0.52	0.54	0.64	0.80	0.06	0.61	0.76	0.56
CaO	52.53	53.12	53.90	53.72	54.55	52.57	53.77	53.38	53.59	53.84
SO_2	1.16	0.32	0.34	0.36	0.39	0.10	0.15	0.45	0.22	0.63
F	2.38	2.36	2.41	2.48	3.16	2.58	2.59	2.68	2.56	2.49
Cl	0.93	1.03	0.87	0.91	0.53	1.06	0.94	0.92	0.96	0.96
OH	0.43	0.74	0.63	0.56	0.29	0.70	0.73	0.71	0.77	0.74
O≡F,Cl,OH	1.41	1.58	1.51	1.51	1.59	1.65	1.65	1.67	1.66	1.61
Total	96.07	97.63	96.93	98.68	99.47	97.01	99.21	98.73	98.46	99.01

Eruption	Astroni 1	Astroni 1	Astroni 1	Astroni 1	Astroni 1	Astroni 1	Astroni 1	Astroni 1	Astroni 1	Astroni 1
Crystal #	CFmap2_CF69_19	CFmap2_CF69_22	CFmap2_CF69_20	CFmap2_CF69_21	CFmap2_CF69_49	CFmap2_CF69_46	CFmap2_CF69_91	CFmap2_CF69_85	CFmap2_CF69_2	CFmap2_CF69_82
Type	mpc	mpc	mpc	mpc	mpc	mpc	mpc	mpc	mpc	Mpc
P_2O_5	41.16	42.17	41.16	41.78	40.05	41.46	40.65	40.64	41.64	41.08
SiO_2	0.67	0.61	0.66	0.62	1.10	0.68	0.64	0.65	0.61	0.74
CaO	53.39	53.78	53.77	53.98	53.01	53.35	53.79	53.86	54.23	53.95
SO_2	0.14	0.16	0.45	0.28	0.18	0.17	0.15	0.69	0.29	0.15
F	2.49	2.51	2.42	2.43	2.61	2.33	2.01	2.56	2.50	2.48
Cl	0.97	0.93	0.95	0.94	1.01	0.99	1.07	0.99	0.98	1.01
OH	0.76	0.77	0.77	0.77	0.79	0.81	0.80	0.57	0.62	0.65
O≡F,Cl,OH	1.62	1.63	1.60	1.60	1.70	1.59	1.46	1.57	1.57	1.58
Total	97.96	99.30	98.58	99.20	97.05	98.20	97.65	98.39	99.30	98.48

Eruption	Astroni 1	Astroni 1	Astroni 1	Astroni 1	Astroni 1	Astroni 1	Astroni 1	Astroni 1	Astroni 1	Astroni 1
Crystal #	CFmap2_CF69_18	CFmap2_CF69_74	CF69_cpx10_ap2	CF69_cpx11_ap1	CF69_cpx32_ap1	CF69_cpx35_ap1	CF69_cpx69_ap1	CF69_cpx73_ap2	CF69_cpx95_ap2	CF69_cpx104_ap1
Type	mpc	mpc	cpx	cpx	cpx	cpx	cpx	cpx	cpx	cpx
P_2O_5	41.04	41.01	41.31	40.99	41.30	41.68	41.24	41.07	40.95	40.50
SiO_2	0.57	0.64	0.68	0.76	0.77	0.66	0.68	0.82	0.67	0.78
CaO	53.67	54.30	54.05	53.92	54.36	54.34	54.09	53.78	53.81	53.95
SO_2	0.40	0.22	0.09	0.32	0.30	0.29	0.15	0.24	0.24	0.29
F	2.57	2.30	2.32	2.13	2.22	2.40	2.36	2.30	2.33	2.34
Cl	1.01	0.57	0.90	0.99	0.92	0.91	0.91	0.88	0.89	0.89
OH	0.60	1.24	0.42	0.58	0.60	0.50	0.53	0.52	0.49	0.47
O≡F,Cl,OH	1.59	1.68	1.37	1.40	1.42	1.45	1.45	1.41	1.41	1.41
Total	98.27	98.60	98.38	98.29	99.05	99.33	98.51	98.20	97.96	97.81

Eruption	Astroni 1	Astroni 1	Astroni 1	Astroni 1	Astroni 1	Astroni 1	Astroni 1	Astroni 1	Astroni 1	Astroni 1
Crystal #	cpx110_ap1	CF69_cpx132_ap1	CF69_cpx137_ap1	CF69_cpx139_ap2	CF69_cpx153_ap2	CF69_cpx151_ap1	CF69_cpx112_ap1	CF69_cpx65_ap2	CF69_cpx21_ap2	CF69_cpx44_ap6
Type	cpx	cpx	cpx	cpx	cpx	cpx	cpx	cpx	cpx	cpx
P_2O_5	41.28	41.13	41.24	41.33	41.18	40.57	41.39	41.33	41.36	40.94
SiO_2	0.64	0.61	0.61	0.57	0.59	0.94	0.50	0.72	0.55	0.56
CaO	53.31	53.37	53.72	54.14	53.71	53.52	54.33	54.62	54.03	53.97
SO_2	0.12	0.38	0.32	0.18	0.33	0.15	0.47	0.17	0.25	0.46
F	2.25	1.86	2.35	2.46	2.22	2.31	2.36	2.45	2.30	2.30
Cl	0.96	0.88	0.89	0.87	1.00	0.92	0.91	0.91	0.96	0.86
OH	0.51	0.46	0.58	0.52	0.68	0.56	0.56	0.58	0.43	0.53
O≡F,Cl,OH	1.40	1.20	1.46	1.48	1.48	1.44	1.46	1.51	1.39	1.41
Total	97.67	97.48	98.24	98.59	98.22	97.53	99.06	99.27	98.50	98.21

Eruption	Astroni 1	Astroni 1	Astroni 1	Astroni 1	Astroni 1	Astroni 1	Astroni 1	Astroni 1	Astroni 1	Astroni 1
Crystal #	CF69_cpx73_ap2	CF69_bt23_ap2	CF69_bt23_ap3	CF69_bt38_ap3	CF69_bt48_ap1	CF69_bt97_ap1	CF69_bt117_ap1	CF69_bt156_ap1	CF69_bt167_ap1	CF69_bt35_ap1
Type	cpx	bt	bt	bt	bt	bt	bt	bt	bt	bt
P_2O_5	41.07	41.60	41.18	41.09	41.14	41.32	41.55	40.85	40.13	41.64
SiO_2	0.82	0.56	0.59	0.69	0.59	0.60	0.53	0.51	0.59	0.47
CaO	53.78	53.97	54.18	53.86	54.14	54.30	54.51	54.49	53.81	54.06
SO_2	0.24	0.34	0.38	0.58	0.31	0.56	0.38	0.40	0.35	0.42
F	2.34	2.40	2.49	2.52	2.42	2.40	2.54	2.37	2.40	2.43
Cl	0.94	0.90	0.93	0.93	0.90	0.92	0.96	0.91	0.88	0.89
OH	0.56	0.59	0.65	0.55	0.66	0.58	0.65	0.57	0.57	0.59
O≡F,Cl,OH	1.46	1.49	1.56	1.53	1.53	1.49	1.59	1.47	1.48	1.50
Total	98.29	98.89	98.85	98.68	98.62	99.19	99.53	98.63	97.26	99.00

Eruption	Astroni 1	Astroni 1	Astroni 1	Astroni 1	Astroni 1	Astroni 1	Astroni 1	Accademia	Accademia	Accademia
Crystal #	CF69_bt27_ap1	CF69_bt149_ap1	CF69_bt98_ap1	CF69_bt164_ap5	CF69_bt164_ap1	CF69_bt158_ap1	CF69_bt170_ap1	CFmap2_CF163_14	CFmap2_CF163_5	CFmap2_CF163_42
Type	bt	bt	bt	bt	bt	bt	bt	mpc	mpc	mpc
P_2O_5	41.78	40.49	40.98	40.95	41.25	41.75	40.97	41.50	40.93	39.97
SiO_2	0.50	0.74	0.58	0.60	0.65	0.45	0.40	0.68	0.51	1.19
CaO	53.99	54.37	53.87	54.35	54.54	54.59	54.01	54.24	53.55	54.42
SO_2	0.29	0.27	0.54	0.27	0.28	0.44	0.40	0.24	0.44	1.01
F	2.38	2.43	2.42	2.48	2.53	2.40	2.40	2.96	3.26	2.22
Cl	0.89	0.90	0.91	0.91	0.93	0.92	0.91	0.66	0.48	0.06
OH	0.53	0.65	0.53	0.66	0.64	0.53	0.53	0.21	0.07	1.62
O≡F,Cl,OH	1.45	1.53	1.48	1.56	1.58	1.47	1.46	1.49	1.51	1.71
Total	98.92	98.32	98.36	98.65	99.25	99.61	98.15	99.00	97.73	98.78

Eruption	Accademia	Accademia	Accademia	Accademia	Accademia	Accademia	Accademia	Accademia	Accademia	Accademia
Crystal #	CFmap2_CF163_25	CFmap2_CF163_24	CFmap2_CF163_28	CFmap2_CF163_20	CFmap2_CF163_46	CFmap2_CF163_39	CFmap2_CF163_32	CFmap2_CF163_8	CFmap2_CF163_6	CFmap2_CF163_11
Type	mpc	mpc	mpc	mpc	mpc	mpc	mpc	mpc	mpc	mpc
P_2O_5	40.90	41.38	41.20	40.94	41.73	40.88	41.21	40.93	40.99	40.68
SiO_2	0.57	0.66	0.77	0.63	0.35	0.77	0.62	0.57	0.58	0.67
CaO	54.08	54.08	53.47	53.47	53.90	53.81	53.64	53.72	53.68	53.35
SO_2	0.54	0.27	0.22	0.17	0.35	0.14	0.16	0.65	0.33	0.25
F	3.62	2.54	2.49	2.61	2.53	2.62	2.52	2.32	2.64	2.63
Cl	0.06	1.04	0.97	1.17	0.89	0.95	0.96	0.89	0.88	1.17
OH	0.01	0.48	0.56	0.36	0.41	0.54	0.56	0.59	0.45	0.51
O≡F,Cl,OH	1.54	1.53	1.53	1.53	1.46	1.57	1.54	1.46	1.52	1.61
Total	98.24	98.92	98.15	97.82	98.70	98.14	98.13	98.21	98.03	97.65

Eruption	Accademia	Accademia	Accademia	Accademia	Accademia	Accademia	Accademia	Santa Maria delle Grazie	Santa Maria delle Grazie	Santa Maria delle Grazie
Crystal #	CFmap2_CF163_10	mpc_CF163__10	mpc-CF163_9	mpc-CF163_8	CFmap2_CF163_100	CFmap2_CF163_63	CFmap2_CF163_12	CF200_map30	CF200_map29	CF200_map35
Type	mpc	mpc	mpc	mpc	mpc	mpc	mpc	mpc	mpc	mpc
P_2O_5	40.51	41.44	40.36	41.10	41.06	41.15	41.37	40.65	40.71	39.27
SiO_2	0.76	0.61	0.82	0.67	0.77	0.60	0.53	0.66	0.61	1.53
CaO	53.20	54.41	53.97	54.22	54.29	54.37	53.97	54.06	53.94	52.93
SO_2	0.23	0.17	0.10	0.23	0.13	0.31	0.16	0.46	0.37	0.24
F	2.83	3.29	3.69	3.78	3.79	3.77	3.60	2.85	3.54	2.67
Cl	0.92	0.09	0.06	0.10	0.05	0.05	0.07	0.68	0.23	1.04
OH	0.46	0.00	0.00	0.00	0.00	0.00	0.00	0.18	0.00	0.33
O≡F,Cl,OH	1.62	1.41	1.57	1.61	1.61	1.60	1.53	1.44	1.54	1.51
Total	97.29	98.60	97.43	98.49	98.48	98.65	98.17	98.10	97.86	96.50

Eruption	Santa Maria delle Grazie	Baia-Fondi di Baia	Baia-Fondi di Baia	Baia-Fondi di Baia	Baia-Fondi di Baia	Baia-Fondi di Baia	Baia-Fondi di Baia	Baia-Fondi di Baia	Baia-Fondi di Baia	Baia-Fondi di Baia
Crystal #	CF200_map36	CFmap1_CF88_42	CFmap1_CF88_49	CFmap1_CF88_34	CFmap1_CF88_16	CFmap1_CF88_11	CFmap1_CF88_10	CFmap1_CF88_18	CFmap1_CF88_33	CFmap1_CF88_43
Type	mpc	mpc	mpc	mpc	mpc	mpc	mpc	mpc	mpc	mpc
P_2O_5	41.14	39.99	40.97	41.23	40.52	40.42	39.43	41.07	39.95	40.29
SiO_2	0.59	0.49	0.50	0.42	0.61	0.54	1.02	0.60	0.94	0.79
CaO	53.86	53.95	54.14	53.98	54.01	54.05	53.80	53.64	52.89	53.19
SO_2	0.33	0.39	0.34	0.43	0.20	0.39	0.90	0.16	0.56	0.13
F	3.57	2.06	2.07	2.29	2.10	2.17	2.18	1.99	1.98	2.32
Cl	0.09	0.85	0.89	0.87	0.86	0.78	0.72	0.87	0.86	0.91
OH	0.00	0.90	1.01	0.95	0.97	0.82	0.88	0.82	0.83	0.91
O≡F,Cl,OH	1.52	1.48	1.55	1.61	1.53	1.48	1.49	1.42	1.42	1.61
Total	98.06	97.15	98.37	98.56	97.74	97.69	97.44	97.73	96.59	96.93

Eruption	Baia-Fondi di Baia	Baia-Fondi di Baia	Baia-Fondi di Baia	Baia-Fondi di Baia	Baia-Fondi di Baia	Baia-Fondi di Baia	Baia-Fondi di Baia	Baia-Fondi di Baia	Baia-Fondi di Baia	Baia-Fondi di Baia
Crystal #	CFmap1_CF88_30	CFmap1_CF88_3	CFmap1_CF88_8	CFmap1_CF88_50	CFmap1_CF88_44	CFmap1_CF88_31	CFmap1_CF88_45	CFmap1_CF88_22	CFmap1_CF88_17	CFmap1_CF88_12
Type	mpc	mpc	mpc	mpc	mpc	mpc	mpc	mpc	mpc	mpc
P_2O_5	41.05	41.61	40.04	39.79	40.04	38.69	40.03	39.84	39.93	40.03
SiO_2	0.40	0.00	0.79	0.86	0.80	1.40	1.00	1.15	1.20	0.97
CaO	54.35	55.46	54.43	53.96	54.28	54.42	53.65	53.36	52.64	53.86
SO_2	0.40	0.00	0.89	0.85	0.77	1.38	0.05	0.48	0.03	0.52
F	2.00	2.50	2.77	2.80	2.34	2.57	3.02	2.69	2.77	2.56
Cl	0.89	0.03	0.09	0.09	0.06	0.04	0.42	0.62	0.55	0.61
OH	0.88	0.92	0.93	0.79	1.16	0.97	0.47	0.63	0.68	0.59
O≡F,Cl,OH	1.46	1.49	1.62	1.57	1.54	1.55	1.59	1.57	1.61	1.49
Total	98.51	99.03	98.32	97.57	97.91	97.92	97.05	97.20	96.19	97.65

Eruption	Baia-Fondi di Baia	Baia-Fondi di Baia	Baia-Fondi di Baia	Baia-Fondi di Baia	Baia-Fondi di Baia	Baia-Fondi di Baia	Baia-Fondi di Baia	Pisani 1	Pisani 1	Pisani 1
Crystal #	CFmap1_CF88_1	CFmap1_CF88_7	CF88_cpx118_ap1	CF88_cpx136_ap1	CF88_cpx85_ap1	CF88_cpx116_ap1	CF88_bt36_ap1	CFmap1_CF25_41	CFmap1_CF25_29	CFmap1_CF25_19
Type	mpc	mpc	cpx	cpx	cpx	cpx	bt	mpc	mpc	mpc
P_2O_5	40.15	40.73	39.71	40.49	40.02	39.79	40.38	40.55	41.63	40.39
SiO_2	0.72	0.45	1.50	1.33	1.25	1.28	1.08	0.77	0.42	0.66
CaO	54.23	54.03	52.48	52.90	53.55	52.78	53.70	53.02	54.27	53.43
SO_2	0.72	0.41	0.00	0.00	0.56	0.00	0.53	0.36	0.37	0.68
F	2.69	2.02	2.79	2.88	2.48	2.84	2.72	2.18	2.14	2.14
Cl	0.61	0.89	0.42	0.43	0.63	0.41	0.54	1.15	0.94	1.10
OH	0.67	0.96	1.03	1.06	1.42	1.00	0.91	0.82	1.04	1.09
O≡F,Cl,OH	1.59	1.50	1.76	1.81	1.86	1.76	1.69	1.56	1.60	1.66
Total	98.20	97.99	96.18	97.28	98.05	96.34	98.16	97.29	99.21	97.83

Eruption	Pisani 1	Pisani 1	Pisani 1	Pisani 1	Pisani 1	Pisani 1	Pisani 1	Pisani 1	Pisani 1	Pisani 1
Crystal #	CFmap1_CF25_7	CFmap1_CF25_44	CFmap1_CF25_5	CFmap1_CF25_2	CFmap1_CF25_22	CFmap1_CF25_30	CFmap1_CF25_18	CFmap1_CF25_46	CFmap1_CF25_37	CFmap1_CF25_50
Type	mpc	mpc	mpc	mpc	mpc	mpc	mpc	mpc	mpc	mpc
P_2O_5	41.14	42.19	39.38	41.82	38.27	38.17	40.64	41.45	42.14	41.11
SiO_2	0.59	0.34	1.16	0.29	1.46	1.59	0.75	0.29	0.24	0.68
CaO	53.65	53.91	54.16	54.10	52.97	53.33	53.70	53.52	54.00	53.91
SO_2	0.69	0.34	1.21	0.06	1.18	1.24	0.63	0.09	0.03	0.13
F	1.96	2.12	2.07	2.83	3.61	3.34	1.98	2.07	2.86	1.95
Cl	1.05	0.92	0.06	0.55	0.12	0.09	0.58	1.00	0.56	0.89
OH	0.95	0.99	1.39	0.35	0.33	0.40	1.21	0.76	0.32	0.96
O≡F,Cl,OH	1.51	1.57	1.54	1.48	1.70	1.61	1.53	1.45	1.48	1.47
Total	98.52	99.24	97.89	98.52	96.24	96.55	97.96	97.73	98.67	98.16

Eruption	Pisani 1	Pisani 1	Pisani 1	Pisani 1	Pisani 1	Pisani 1	Pisani 1	Pisani 1	Pisani 1	Pisani 1
Crystal #	CFmap1_CF25_11	CFmap1_CF25_9	CFmap1_CF25_3	CFmap1_CF25_1	CFmap1_CF25_16	CFmap1_CF25_27	CFmap1_CF25_49	CF25_cpx98_ap2	CF25_cpx98_ap5	CF25_cpx121_ap1
Type	mpc	mpc	mpc	mpc	mpc	mpc	mpc	cpx	cpx	cpx
P_2O_5	39.29	39.66	40.88	42.41	42.02	42.09	41.94	40.79	40.22	40.04
SiO_2	0.91	1.10	0.67	0.00	0.24	0.25	0.24	0.40	0.78	0.54
CaO	53.46	53.41	54.32	54.89	53.88	54.21	54.03	54.44	54.04	53.77
SO_2	1.28	0.38	0.67	0.02	0.05	0.09	0.03	0.25	0.58	0.63
F	2.02	2.58	1.96	2.59	3.03	2.93	2.80	1.92	1.92	2.03
Cl	1.10	0.74	1.00	0.02	0.45	0.06	0.51	0.82	0.91	1.02
OH	0.90	0.69	0.93	0.99	0.28	0.44	0.48	1.01	1.01	1.04
O≡F,Cl,OH	1.52	1.58	1.49	1.56	1.51	1.45	1.52	1.47	1.49	1.58
Total	97.44	96.98	98.94	99.36	98.44	98.62	98.51	98.16	97.97	97.50

Eruption	Pisani 1	Pisani 1	Pisani 1	Pisani 1	Pisani 1	Pisani 1	Pisani 1	Pomici Principali	Pomici Principali	Pomici Principali
Crystal #	CF25_cpx122_ap1	CF25_cpx142_ap2	CF25_bt40_ap1	CF25_bt67_ap2	CF25_bt98_ap1	CF25_bt112_ap1	CF25_bt110_ap1	CFmap2_CF6_33	CFmap2_CF6_37	CFmap2_CF6_39
Type	cpx	cpx	bt	bt	bt	bt	bt	mpc	mpc	mpc
P_2O_5	40.88	40.68	41.56	40.36	41.27	39.20	41.47	40.86	38.06	41.25
SiO_2	0.40	0.42	0.37	0.39	0.49	0.50	0.37	0.77	1.86	0.66
CaO	54.52	54.45	54.81	54.55	54.81	54.46	54.13	53.59	52.96	54.30
SO_2	0.46	0.37	0.37	0.42	0.46	0.36	0.31	0.79	1.48	0.66
F	1.89	1.96	2.07	1.93	1.93	2.03	2.03	3.80	2.94	1.89
Cl	0.89	1.00	1.01	0.84	0.84	0.99	1.01	0.03	0.07	0.58
OH	1.10	0.81	0.93	1.20	0.97	1.04	0.90	0.24	1.21	1.97
O≡F,Cl,OH	1.52	1.44	1.54	1.57	1.46	1.57	1.50	1.72	1.82	1.85
Total	98.63	98.25	99.57	98.12	99.31	97.02	98.72	98.36	96.76	99.46

Eruption	Pomici Principali	Pomici Principali	Pomici Principali	Pomici Principali	Pomici Principali	Pomici Principali	Pomici Principali	Pomici Principali	Pomici Principali	Pomici Principali
Crystal #	CFmap2_CF6_47	CFmap2_CF6_25	CFmap2_CF6_24	CFmap2_CF6_30	CFmap2_CF6_32	CFmap2_CF6_16	CFmap2_CF6_10	CFmap2_CF6_13	CFmap2_CF6_6	CFmap2_CF6_5
Type	mpc	mpc	mpc	mpc	mpc	mpc	mpc	mpc	mpc	mpc
P_2O_5	41.61	41.66	41.79	42.03	40.00	40.46	41.71	41.03	42.00	42.06
SiO_2	0.49	0.52	0.48	0.35	1.29	0.70	0.52	0.60	0.60	0.39
CaO	54.18	54.00	54.34	54.16	52.40	53.33	53.74	53.92	54.04	54.16
SO_2	0.38	0.39	0.44	0.48	0.18	0.23	0.34	0.75	0.22	0.43
F	1.90	2.66	2.43	2.14	2.40	2.10	2.06	2.07	2.07	2.08
Cl	0.63	0.65	0.76	0.75	1.02	0.89	0.88	1.01	0.91	0.90
OH	1.50	0.91	1.01	1.31	1.16	1.09	1.12	1.12	1.15	1.14
O≡F,Cl,OH	1.65	1.69	1.67	1.69	1.79	1.60	1.59	1.63	1.62	1.62
Total	99.04	99.10	99.58	99.53	96.66	97.20	98.78	98.87	99.37	99.54

Eruption	Pomici Principali	Pomici Principali	Pomici Principali	Pomici Principali	Pomici Principali	Pomici Principali	Pomici Principali	Pomici Principali	Pomici Principali	Pomici Principali
Crystal #	CFmap2_CF6_46	CFmap2_CF6_21	CFmap2_CF6_100	CFmap2_CF6_15	CFmap2_CF6_26	CFmap2_CF6_98	CFmap2_CF6_92	CFmap2_CF6_62	CF6_cpx19_ap1	CF6_cpx64_ap1
Type	mpc	mpc	mpc	mpc	mpc	mpc	mpc	mpc	cpx	cpx
P_2O_5	41.36	42.04	39.99	41.04	41.45	40.93	40.23	40.05	41.35	40.50
SiO_2	0.67	0.42	1.17	0.53	0.48	0.65	1.10	1.11	0.43	0.68
CaO	53.89	53.64	52.68	53.97	53.87	54.01	53.31	54.96	54.66	53.97
SO_2	0.77	0.34	0.07	0.75	0.44	0.72	0.19	1.09	0.27	0.52
F	2.21	2.06	2.39	2.12	2.84	2.06	1.97	2.20	2.08	2.00
Cl	1.11	0.90	1.05	1.04	0.75	1.00	0.95	0.07	0.85	0.97
OH	0.95	1.02	0.85	0.88	0.19	0.89	0.99	1.30	0.93	1.35
O≡F,Cl,OH	1.63	1.55	1.64	1.54	1.45	1.51	1.51	1.55	1.51	1.70
Total	99.33	98.87	96.56	98.79	98.57	98.75	97.23	99.23	99.06	98.28

Eruption	Pomici Principali	Pomici Principali	Pomici Principali	Pomici Principali	Pomici Principali	Minopoli 1	Minopoli 1	Minopoli 1	Minopoli 1	Minopoli 1
Crystal #	CF6_cpx96_ap1	CF6_cpx138_ap1	CF6_bt94_ap1	CF6_bt112_ap1	CF6_bt26_ap1	CFmap1_CF13_39	CFmap1_CF13_50	CFmap1_CF13_15	CFmap1_CF13_16	CFmap1_CF13_3
Type	cpx	cpx	bt	bt	bt	mpc	mpc	mpc	mpc	mpc
P_2O_5	40.30	40.41	40.31	40.72	40.75	40.93	40.66	40.58	39.82	40.85
SiO_2	0.70	0.96	0.93	0.68	0.76	0.60	0.48	0.89	0.75	0.37
CaO	53.58	53.94	53.39	54.16	54.04	54.34	54.54	53.57	53.63	54.34
SO_2	0.51	0.64	0.60	0.51	0.55	0.63	0.18	0.81	0.81	0.36
F	2.14	1.94	2.26	2.22	2.27	2.16	3.11	2.27	1.94	2.03
Cl	0.93	0.90	0.95	0.97	0.97	0.55	0.03	0.74	0.63	1.08
OH	0.82	1.08	1.14	1.16	1.18	1.08	0.39	1.51	1.38	0.78
O≡F,Cl,OH	1.50	1.53	1.70	1.70	1.73	1.54	1.50	1.83	1.61	1.47
Total	97.47	98.34	97.87	98.72	98.80	98.75	97.89	98.54	97.35	98.34

Eruption	Minopoli 1	Minopoli 1	Minopoli 1	Minopoli 1	Minopoli 1	Minopoli 1	Minopoli 1	Minopoli 1	Minopoli 1	Minopoli 1
Crystal #	CFmap1_CF13_4	CFmap1_CF13_7	CFmap1_CF13_22	CFmap1_CF13_31	CFmap1_CF13_27	CFmap1_CF13_2	CFmap1_CF13_10	CFmap1_CF13_42	CFmap1_CF13_19	CFmap1_CF13_8
Type	mpc	mpc	mpc	mpc	mpc	mpc	mpc	mpc	mpc	mpc
P_2O_5	39.50	40.81	40.04	41.03	40.78	40.13	40.70	41.37	41.39	42.39
SiO_2	0.84	0.51	1.20	0.42	0.63	1.00	0.45	0.41	0.50	0.06
CaO	54.03	53.92	53.26	54.06	53.77	52.90	53.86	53.81	54.92	54.64
SO_2	0.74	0.59	0.17	0.44	0.33	0.19	0.31	0.42	0.47	0.00
F	2.24	2.08	1.94	1.83	2.86	2.08	2.00	1.96	1.71	2.84
Cl	0.05	0.85	0.90	0.81	0.93	0.94	0.88	0.86	0.41	0.12
OH	1.35	1.01	1.10	0.98	0.24	1.04	0.97	0.88	1.29	0.51
O≡F,Cl,OH	1.59	1.54	1.54	1.41	1.53	1.58	1.50	1.43	1.42	1.46
Total	97.16	98.23	97.07	98.16	98.01	96.70	97.67	98.28	99.27	99.10

Eruption	Minopoli 1	Minopoli 1	Minopoli 1	Minopoli 1	Minopoli 1	Minopoli 1	Minopoli 1	Minopoli 1		
Crystal #	CFmap1_CF13_30	CFmap1_CF13_43	CFmap1_CF13_28	CFmap1_CF13_41	CFmap1_CF13_49	CFmap1_CF13_32	CF13_cpx1 69_ap1	CF13_bt11 4_ap1		RP
Type	mpc	mpc	mpc	mpc	mpc	mpc	cpx	bt		
P_2O_5	38.93	40.24	40.59	39.39	41.19	41.08	41.91	41.47		0.45
SiO_2	1.34	0.60	0.58	1.20	0.39	0.53	0.42	0.55		0.05
CaO	54.05	54.82	53.61	54.10	53.81	54.51	54.40	54.15		0.50
SO_2	1.36	0.44	0.74	0.97	0.11	0.44	0.41	0.55		0.03
F	2.45	3.24	2.32	1.81	2.02	2.12	1.94	1.94		0.18
Cl	0.06	0.02	0.56	0.48	0.70	0.88	0.76	0.83		0.15
OH	1.30	0.45	0.97	1.37	0.81	1.01	0.89	1.06		0.08
O≡F,Cl,OH	1.66	1.58	1.56	1.51	1.39	1.57	1.41	1.50		
Total	97.83	98.23	97.81	97.81	97.64	99.00	99.32	99.04		

Table 3. Major and volatile element analyses of representative Campi Flegrei apatite inclusions and microphenocrysts. Halogens and OH were measured by SIMS, all other elements were measured by EPMA. Crystal type refers to textural association: cpx, clinopyroxene-hosted inclusion; bt, biotite-hosted inclusion; mpc, microphenocryst. Concentrations are in wt%. RP is representative absolute precision with one standard deviation based on counting statistics for elements measured by EPMA, and a 95% confidence interval based on regression of calibration standards for elements measured by SIMS.